

# Charged particle dynamics and distribution functions in low pressure dual-frequency capacitively coupled plasmas operated at low frequencies and high voltages

P Hartmann<sup>1,2</sup> , L Wang<sup>3,4</sup> , K Nösges<sup>3</sup>, B Berger<sup>3</sup> , S Wilczek<sup>3</sup> ,  
R P Brinkmann<sup>3</sup>, T Mussenbrock<sup>5</sup> , Z Juhasz<sup>6</sup>, Z Donkó<sup>1</sup> , A Derzsi<sup>1</sup> ,  
Eunwoo Lee<sup>7</sup> and J Schulze<sup>3,4,8</sup> 

<sup>1</sup> Institute for Solid State Physics and Optics, Wigner Research Centre for Physics, H-1121 Budapest, Konkoly-Thege Miklós str. 29-33, Hungary

<sup>2</sup> Center for Astrophysics, Space Physics, and Engineering Research, Baylor University, One Bear Place 97310, Waco, Texas 76798, United States of America

<sup>3</sup> Department of Electrical Engineering and Information Science, Ruhr-University Bochum, D-44780, Bochum, Germany

<sup>4</sup> Key Laboratory of Materials Modification by Laser, Ion, and Electron Beams (Ministry of Education), School of Physics, Dalian University of Technology, Dalian 116024, People's Republic of China

<sup>5</sup> Electrodynamics and Physical Electronics Group, Brandenburg University of Technology Cottbus-Senftenberg, Cottbus 03046, Germany

<sup>6</sup> Department of Electrical Engineering and Information Systems, University of Pannonia, H-8200 Hungary

<sup>7</sup> Samsung Electronics Co., Ltd., 1 Samsungjeonja-ro, Hwaseong-si, Gyeonggi-do 18448, Republic of Korea

E-mail: [schulze@aept.ruhr-uni-bochum.de](mailto:schulze@aept.ruhr-uni-bochum.de)

Received 26 February 2020, revised 1 May 2020

Accepted for publication 15 May 2020

Published 28 July 2020



CrossMark

## Abstract

In high aspect ratio (HAR) dielectric plasma etching, dual-frequency capacitively coupled radio-frequency plasmas operated at low pressures of 1 Pa or less are used. Such plasma sources are often driven by a voltage waveform that includes a low-frequency component in the range of hundreds of kHz with a voltage amplitude of 10 kV and more to generate highly energetic vertical ion bombardment at the wafer. In such discharges, the energetic positive ions can overcome the repelling potential created by positive wall charges inside the etch features, which allows high aspect ratios to be reached. In order to increase the plasma density a high-frequency driving component at several 10 MHz is typically applied simultaneously. Under such discharge conditions, the boundary surfaces are bombarded by extremely energetic particles, of which the consequences are poorly understood. We investigate the charged particle dynamics and distribution functions in this strongly non-local regime in argon discharges by particle-in-cell simulations. By including a complex implementation of plasma-surface interactions, electron induced secondary electron emission ( $\delta$ -electrons) is found to have a strong effect on the ionization dynamics and the plasma density. Due to the high ion energies at the electrodes, very high yields of the ion induced secondary electron emission ( $\gamma$ -electrons) are found. However, unlike in classical capacitive plasmas, these  $\gamma$ -electrons do not cause significant ionization directly, since upon acceleration in the high voltage sheaths, these electrons are too energetic to ionize the neutral gas efficiently. These  $\gamma$ - and  $\delta$ -electrons as well as electrons created in the plasma bulk and accelerated

<sup>8</sup> Author to whom any correspondence should be addressed.

towards the electrodes to high energies by reversed electric fields during the local sheath collapse are found to induce the emission of a high number of  $\delta$ -electrons, when they hit boundary surfaces. This regime is understood fundamentally based on the following approach: first, dual-frequency discharges with identical electrode materials are studied at different pressures and high-frequency driving voltages. Second, the effects of using electrodes made of different materials and characterized by different secondary electron emission coefficients are studied. The electron dynamics and charged particle distribution functions at boundary surfaces are determined including discharge asymmetries generated by using different materials at the powered and grounded electrodes.

Keywords: capacitively coupled plasmas, low-frequency and high voltage discharges, plasma-surface interactions

(Some figures may appear in colour only in the online journal)

## 1. Introduction

Capacitively coupled plasmas (CCPs) are widely used as surface etching, deposition and sputtering devices in microelectronics manufacturing due to their simple geometry and their ability to generate large area and radially uniform plasmas [1–3]. In CCPs used for high aspect ratio (HAR) plasma etching in semiconductor fabrication, energetic positive ions are required to reach the bottom of the etch trenches with a narrow angular distribution, which is made possible by their acceleration towards the wafer by the sheath electric field. As some ions do not impact the wafer vertically, but under some angle with respect to the surface normal, also the sidewalls of the HAR trenches are bombarded by positive ions. In contrast to the positive ions, electrons reach the wafer surface only during the local sheath collapse and with a broad angular distribution. These electrons are typically not accelerated towards the bottom of the trenches. As a result, the bottom (and the sidewalls) of etch trenches can charge up positively due to positive ion bombardment so that electric fields are generated inside the trenches which can decelerate or deflect positive ions and can lead to etch stop, notching, twisting, and tilting [4, 5]. In order to obtain good HAR etch features and to realize high aspect ratios, extremely high ion energies (thousands of eV) are required to overcome the potential barrier generated by the positive surface charges inside the trenches. This requires very high driving voltage amplitudes of several kV and collisionless sheaths to realize high energy and vertical ion bombardment at the wafer. In order to apply such high voltages, low frequencies in the kHz range must be used.

In low pressure single-frequency discharges, using such low frequencies and high voltages results in very large sheaths due to the low plasma density caused by the inefficient electron heating at low driving frequencies. Due to the large sheaths, frequent collisions between ions and atoms occur in the sheaths and the ion flux-energy distribution function at the wafer is collisional, i.e. the high energy tail required for etching is depleted. Moreover, strong gas heating by energetic ions accelerated by the sheath electric field in the entire electrode gap happens and this can cause instabilities in such discharges.

Adding a second component with a much higher frequency to the driving voltage waveform in the range of several 10 MHz solves this problem [6, 7]. In such dual-frequency discharges, much higher plasma densities and smaller sheaths are obtained. This keeps the discharge stable and ensures collisionless sheaths as well as energetic vertical ion bombardment at the wafer. Similar discharge conditions are used for HAR dielectric plasma etching in CCPs [8–15]. The interest in this low-frequency and high voltage operation regime is the motivation of our studies.

The charged particle bombardment energy and angular distributions at the surfaces are known to play an important role for the etch yield, but at the same time can greatly influence other aspects of the plasma surface interaction as well [16, 17]. In recent years, effects of the surfaces on the plasma have been in the focus of interest. Realistic energy and material dependent secondary electron emission (SEE) was found to have a remarkable influence on the discharge [18–21]. In high voltage discharges, ions accelerated by the sheath electric field can gain very high bombarding energies and can generate large numbers of secondary electrons at the electrode surfaces. These ion induced secondary electrons ( $\gamma$ -electrons) can change the electron power absorption and ionization dynamics greatly under certain discharge conditions [22, 23]. Belenguer *et al* [24] reported that  $\gamma$ -electrons can cause a heating mode transition from the  $\alpha$ -mode [25–27] to the  $\gamma$ -mode [28] at high driving voltages and/or gas pressures. In dual-frequency discharges,  $\gamma$ -electrons were found to significantly affect the quality of the separate control of the ion flux and mean energy at the electrodes [29, 30]. Previous studies have shown that besides positive ions, fast neutrals, metastable atoms and VUV photons can also contribute to secondary electron emission [31, 32]. The relative contribution of each process depends on the discharge conditions and the electrode surface properties.

In discharges operated at low pressures and high voltages, the heavy particle induced secondary electrons generated at one electrode are accelerated by the local sheath electric field, propagate through the bulk region, and bombard the opposite electrode at high energies. Consequently, complex electron-surface interactions, including elastic reflection,

inelastic backscattering and electron induced secondary electron emission can happen and can play an important role. In some recent studies, the importance of these electron-surface interactions has been addressed by incorporating realistic surface models into simulations. Horváth *et al* analyzed the effects of electron induced secondary electrons ( $\delta$ -electrons) from SiO<sub>2</sub> electrodes in single-frequency CCPs driven at 13.56 MHz [33]. Through comparing the results obtained from a complex and a simplified model, where only the elastic reflection of electrons at the electrodes was taken into account with a constant probability, different electron power absorption and ionization dynamics were identified. The results from the complex model reveal that  $\delta$ -electrons play a key role in the electron power absorption and ionization dynamics. In their following work, the influence of  $\delta$ -electrons on the ionization dynamics and plasma parameters at various pressures, voltage amplitudes and ion induced secondary electron emission coefficients ( $\gamma$ -coefficients) was studied [34]. These parameters were found to largely affect the role of the  $\delta$ -electrons in the discharge. These authors also pointed out that the effect of  $\delta$ -electrons on the ionization dynamics is most striking at low pressures, high voltage amplitudes and high values of the  $\gamma$ -coefficient. At such conditions a significant fraction of the total ionization can be caused by the  $\delta$ -electrons.

In the presence of strongly electron emitting surfaces, Campanell *et al* [35, 36] found that ‘inverse sheaths’ are generated in the vicinity of these boundary surfaces. Within these regions reversed electric fields accelerate electrons towards the electrode. In this way the positive ion flux to such strongly emitting electrodes can be compensated on time average, since some of the emitted electrons are pulled back towards the surface, where they are absorbed.

In CCP discharges, the electrode surface material plays an important role, since it influences the plasma properties through both chemical and physical processes [37–39]. One important aspect is the SEE from the surfaces [34, 40]. Both the ion induced and the electron induced secondary electron emission coefficients show a strong dependence on the surface material characteristics, which can affect the discharge operation strongly. Operating such discharges between electrodes made of different materials can even induce an asymmetry of the discharge. Recent works showed that different secondary electron emission coefficients and/or electron reflection probabilities at the grounded and powered electrodes can induce an asymmetry effect and the generation of a dc self-bias [41, 42]. Therefore, using a material and energy dependent SEE model in simulations of such plasmas is very important.

In this work, we investigate the charged particle dynamics and distribution functions in low pressure dual-frequency CCPs driven by the superposition of harmonic waveforms with a low driving frequency (400 kHz) and a high driving frequency (40 MHz) by 1d3v particle-in-cell/Monte Carlo collisions (PIC/MCC) simulations. The amplitude of the low-frequency component is kept constant at 10 kV, while the amplitude of the high-frequency component is varied between 1000 V and 2400 V. Our simulation code

includes a complex treatment of plasma-surfaces interactions via material specific and energy dependent SEE coefficients for heavy particles (ions and fast atoms) and electrons. The simulations are performed in argon gas to minimize the complexity of the plasma chemistry. In this way we reveal how such CCPs operate under conditions to some extent relevant for HAR plasma etching and how process relevant energy and angular distribution functions are formed at boundary surfaces. We find that the spatio-temporal ionization dynamics is different compared to that in conventional CCPs driven at lower voltages. A complex interplay of heavy particle and electron induced secondary electrons emitted and accelerated to high energies at distinct times within the low-frequency RF period as well as bulk electrons is found to dominate the ionization dynamics. Due to this strong dependence of the plasma generation on the choice of the electrode material, significant discharge asymmetries are found to be induced by using different electrode surface materials at the powered and grounded side, respectively. This asymmetry is found to affect process relevant energy and angular distribution functions of charged particles at boundary surfaces. These results provide the basis for knowledge based process optimization in CCPs operated under similar conditions.

This paper is structured in the following way: in section 2, a detailed description of the PIC/MCC simulation is provided, including a description of the treatment of gas phase processes, surface processes and the calculation of the electric field as well as the neutral gas temperature. The simulation results are presented in section 3, which consists of two parts: dual-frequency discharges with identical electrode materials are studied in section 3.1, while the effect of different surface materials is discussed in section 3.2. Concluding remarks are given in section 4.

## 2. PIC/MCC simulation

The development of the particle-in-cell (PIC) simulation method started already in the 1950s to study the behaviour of hydrodynamic systems [43]. The popularity of the PIC method in the field of gas discharge physics started to increase rapidly after Birdsall and Langdon [44, 45] adopted it to electrically charged particle systems. They also incorporated a Monte-Carlo type collision (MCC) treatment of the interactions between charged particles and the thermal background gas into the simulation scheme. The resulting ‘PIC/MCC’ approach has become the most widespread method for numerical kinetic studies of CCPs over the past decades [44–53]. Recent improvements in computing capabilities, e. g. those provided by graphic processing units (GPUs), led to a drastic shortening of simulation times and made time-consuming problems tractable [54–56].

Here, we perform PIC/MCC simulations of a CCP in argon gas, with a few types of ‘active’ species and with a restricted number of elementary processes. The active species in the code are electrons, Ar<sup>+</sup> ions and Ar<sup>f</sup> fast neutral atoms. The motion of these particles under the influence of the electric field and their interactions with the background of thermal argon atoms is followed. These particles originate both from

gas-phase and surface reactions. Electrons can be created by ions, fast neutrals and electrons at the electrode surfaces and can be born as well in ionization processes in the volume. The latter process is the source of argon ions, which, in elastic collisions (which are considered to have an isotropic and a charge exchange channel) with thermal background gas atoms can create fast neutrals. Neutrals are defined to be ‘fast’ provided that their kinetic energy exceeds nine times the thermal energy [57].

The CCPs investigated here are driven by the superposition of two harmonic waveforms with a low driving frequency of  $f_{lf} = 400$  kHz and a high driving frequency of  $f_{hf} = 40$  MHz. The amplitude of the low-frequency component is kept constant at  $V_{lf} = 10$  kV, while the amplitude of the high-frequency component,  $V_{hf}$ , is varied between 1000 V and 2400 V. The pressure  $p$  is between 0.5 and 1.5 Pa, the electrode gap is  $L = 5$  cm. The high voltage amplitudes require simulation settings that would result in convergence times of many months of a sequential program on a modern CPU. This is mainly caused by the need for extremely small simulation time-steps due to the fact that electrons with very high energies of over 10 keV are generated in the discharge at the conditions studied. Besides, the resulting high plasma density requires a high spatial resolution that also calls for the use of a high number of simulation particles. To cope with this problem, we have ported our one dimensional electrostatic PIC/MCC code (see e. g. reference [49]) to GPU architecture utilising the CUDA programming language extension.

As this is the first work conducted with our upgraded simulation code, both the physical model and the implementation are introduced in detail in the following subsections, which follow the structure of the PIC/MCC scheme and consist of: (i) gas-phase processes involving the interactions of electrons,  $\text{Ar}^+$  single charged ions and  $\text{Ar}^f$  fast neutral atoms with the atoms of the background argon gas; (ii) the absorption and emission processes at the electrodes; (iii) the self-consistent electric field and gas temperature calculation.

## 2.1. Gas phase processes

One of the principal approximations of the PIC method is that the vast amount of real microscopic particles, such as electrons and ions present in the discharge gap, is reduced by using ‘super-particles’, each representing a given number of real particles. The ratio of the real particle number and the superparticle number is defined by the weight factor  $w$ . This factor can be used to find the optimal balance between accuracy and simulation time.

The tasks to be dealt with in the gas phase are: (i) the propagation of the super-particles (referred to as particles in the following); (ii) binary collisions between the particles and the background gas; (iii) energy deposition to (heating of) the background gas. In the simulations, a single  $w$  weight factor is used for all particle species and cases studied.

**2.1.1. Particle pusher.** The motion of the particles in the discharge gap is realized by solving their Newton’s equation of motion in an electric field  $E(x, t)$ , where  $x$  is the only rel-

evant spatial coordinate and  $t$  is the time. The electric field is computed self-consistently on a numerical mesh solving the Poisson equation with proper boundary conditions and the actual distribution of the charged particles, as detailed in section 2.3. We have implemented the leap-frog algorithm to find the particle trajectories, which uses discretization of time by introducing the time-step  $\Delta t$ . This time-step needs to fulfill some stability and accuracy criteria in order to provide reliable numerical results. The intrinsic plasma oscillations have to be properly resolved, therefore  $\Delta t < 0.2/\omega_p$  must hold, where  $\omega_p$  is the electron plasma frequency. The probability of a collision to occur in a  $\Delta t$  time-step must be small. This leads to the restriction of  $\Delta t < 0.05/\nu_{\max}$ , where  $\nu_{\max}$  is the maximum value of the energy-dependent total collision frequency. The Courant condition must be fulfilled, i. e. even the fastest particle shall not travel more than one numerical grid cell distance (labeled  $\Delta x$ , see section 2.3) in one time-step, thus  $\Delta t < \Delta x/v_{\max}$ , where  $v_{\max}$  can be approximated by the velocity of an electron that has been accelerated by the maximum applied voltage. It turns out that under the conditions relevant to the present study (high voltage, low pressure) the Courant condition is the most restrictive criterion requiring time-steps as short as  $\Delta t = 0.6$  ps, which is almost two orders of magnitude shorter than what was used in our earlier studies of lower voltage discharges, making the new implementation with GPU acceleration necessary. This is mostly caused by the presence of extremely energetic electrons. In the simulations, a single  $\Delta t$  time-step is used for all particle species.

**2.1.2. Monte Carlo collisions.** In the simulations, electrons,  $\text{Ar}^+$  ions and  $\text{Ar}^f$  fast neutral atoms are traced in the background of argon atoms at a given pressure  $p$  with a distribution of the gas temperature given by  $T(x)$ . The probability of a collision to occur, while a particle is moving a small distance of  $\Delta s$  with kinetic energy  $\varepsilon$  is  $P(\Delta s) = 1 - \exp[-n(p, T)\sigma(\varepsilon)\Delta s]$ , where  $n(p, T) = p/(k_B T)$  is the pressure and temperature dependent gas density with  $k_B$  being the Boltzmann constant, and  $\sigma(\varepsilon)$  is the cross-section of a given elementary collision process. The technical details of how the colliding particles are selected, how the type of collision is chosen, and how this process is accelerated using the null-collision method can be found in reference [49] and references therein.

A key aspect in these kinds of Monte Carlo collision models is the choice and availability of coherent sets of cross-sections that can properly reproduce particle transport. In our case we have included elastic scattering, excitation to 25 individual energy levels, and ionization for electrons; elastic scattering with an isotropic and a backward channel (charge exchange), excitation to 3 individual energy levels, and ionization for  $\text{Ar}^+$  ions; and elastic scattering, excitation to 3 individual energy levels, and ionization for  $\text{Ar}^f$  fast neutral atoms. The details of the implementation of these collision processes follow.

For elastic electron + Ar collisions we use the total elastic cross-section from the complex optical potential (COP)

database [58, 59], which we have implemented after successful validation of the data with independent experimental and theoretical sources [63–67]. Cross-section data for inelastic collisions (excitation and ionization) are taken from the Hayashi database [60, 61], the complete set of electron collision cross-sections is shown in figure 1(a). We apply the cold gas model in case of electron + Ar collisions, thus the thermal motion of the background Ar atoms is neglected. For both the elastic and the excitation processes we apply anisotropic scattering, where the scattering angle  $\chi$  is assigned based on the screened-Coulomb model as discussed in [68]:

$$\cos \chi = 1 - \frac{2R_{01}(1 - \xi)}{1 + \xi(1 - 2R_{01})}, \quad (1)$$

where  $R_{01}$  is a random number with uniform distribution between 0 and 1 and  $\xi = 4\varepsilon/(1 + 4\varepsilon)$ , with  $\varepsilon$  being the kinetic energy of the electron after the collision including energy losses due to excitations. The azimuth angle is assigned randomly as  $\varphi = 2\pi R_{01}$ . In case of ionization, the energy of the impacting electron ( $\varepsilon_0$ ) is reduced by the ionization energy ( $\varepsilon_{\text{ion}} = 15.8$  eV in this case), and the remaining kinetic energy is shared between the scattered impacting ( $\varepsilon_1$ ) and the new emitted ( $\varepsilon_2$ ) electrons as:

$$\varepsilon_2 = \tilde{\varepsilon} \tan \left[ R_{01} \tan^{-1} \left( \frac{\varepsilon_0 - \varepsilon_{\text{ion}}}{2\tilde{\varepsilon}} \right) \right], \quad (2)$$

$$\varepsilon_1 = \varepsilon_0 - \varepsilon_{\text{ion}} - \varepsilon_2,$$

where  $\tilde{\varepsilon} = 15$  eV, as it is introduced in [69] on the basis of experimental [70] and theoretical [71] data and discussed in [72]. The scattering angles are assigned with keeping the conservation of momentum in mind as  $\cos \chi_1 = \sqrt{\varepsilon_1/(\varepsilon_0 - \varepsilon_{\text{ion}})}$  and  $\cos \chi_2 = \sqrt{\varepsilon_2/(\varepsilon_0 - \varepsilon_{\text{ion}})}$ . The first azimuth angle is chosen randomly and the second is obtained from  $\varphi_2 = \pi + \varphi_1$ .

In case of heavy particle ( $\text{Ar}^+$  and  $\text{Ar}^f$ ) collisions, the initial velocity of the target background Ar atom is sampled randomly from a Maxwell–Boltzmann velocity distribution with the gas temperature at the position of the collision. The cross-section data are taken from reference [62], which includes both elastic and inelastic processes, as shown in figure 1(b) for ions and in figure 1(c) for fast neutrals. All these collisions, except for the charge transfer process, are implemented with an isotropic scattering profile in the center-of-mass frame for the impacting particle, while the conservation of momentum principle defines the velocity of the target atom after the collision. In case of ionization, the electrons are emitted at 0.5 eV energy in random directions. The symmetric charge transfer process yields a fast atom and a slow (thermal) ion as scattering products, where the  $\text{Ar}^f$  particle inherits the total energy and momentum of the impacting ion, representing the most important process for ‘primary’ fast atom creation, which can induce avalanches creating hundreds of fast neutrals in further collisions with other background atoms.

Electrons that are emitted from an atom by any of the three possible ionization processes in the gas are labeled ‘bulk-

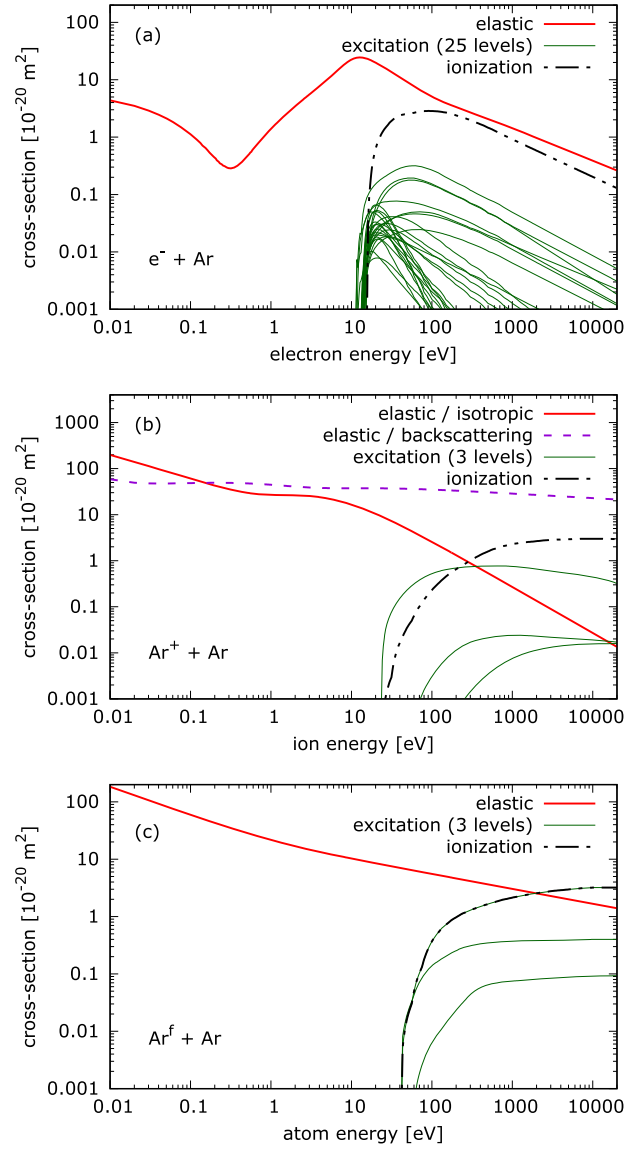


**Figure 1.** Cross-sections included in the model for: (a) electron + Ar [58–61]; (b)  $\text{Ar}^+ + \text{Ar}$  [62], and (c)  $\text{Ar}^f + \text{Ar}$  [62] collisions. The energy is given in the laboratory frame.

electrons’, which label is used for diagnostic purposes only and remains with the electron until it is absorbed at one of the electrodes.

**2.1.3. Gas heating.** In every heavy particle collision the velocity of the background gas atom is altered. If the kinetic energy of a fast atom after a collision falls below the threshold energy that defines a neutral to be fast, i.e.  $\varepsilon_{\text{after}} < 9\frac{3}{2}k_B T(x)$  then its energy gain  $\varepsilon_{\text{after}} - \varepsilon_{\text{init}}$  is added to the heating energy function  $\tilde{S}_{\text{heat}}(x)$  with proper sign. If a background Ar atom is given large enough energy in a collision process so that  $\varepsilon_{\text{after}} > 9\frac{3}{2}k_B T(x)$ , the particle is added to the pool of fast atoms, which are traced in the simulation and its initial kinetic energy  $\varepsilon_{\text{init}}$  (randomly sampled from a Maxwell–Boltzmann distribution) is subtracted from  $\tilde{S}_{\text{heat}}(x)$ . If in any further collision the energy of a fast neutral drops below the  $9\frac{3}{2}k_B T(x)$  limit, it is removed from the particle lists and its energy is added to the heating energy function. The contributions of

the individual particles to the heating energy function are accumulated over a defined time duration (typically one low-frequency RF cycle:  $T_{\text{lf}}$ ) and the heating power distribution function is obtained simply as  $S_{\text{heat}}(x) = S_{\text{heat}}(x)/T_{\text{lf}}$ .

## 2.2. Surface processes

All particles that are traced in the discharge gap at some point hit one of the electrode surfaces. In this case there are several options that are considered in the simulation which are sampled following the Monte Carlo principles by using random numbers and physically relevant distributions.

Heavy particles ( $\text{Ar}^+$  and  $\text{Ar}^f$ ) arriving at the electrodes loose their charge and kinetic energy (without contributing to gas heating), and can induce SEE. The probability of electron emission is given by the impact energy dependent yields  $\gamma_{\text{ion}}(\varepsilon)$  and  $\gamma_{\text{atom}}(\varepsilon)$  adopted from reference [73] and depicted in figure 2(a). There are two sets of yield functions included in the model, one for ‘clean metals’ and one for ‘dirty metals’, as referred to in reference [73]. The former is used in case of pure materials (Si in our case), while the latter is used for oxides ( $\text{SiO}_2$  in the present work). Due to the lack of more specific data for heavy particle induced SEE coefficients (SEEC) for Si/ $\text{SiO}_2$ , this approach is expected to provide realistic results. Changes of the absolute values of these surface coefficients will not change the qualitative findings of this work as long as the general dependence of the SEEC on the incident particle energy is maintained and different electrode materials are characterized by different SEECs. Electrons that are emitted from the surface by heavy particle impact emission are labeled ‘ $\gamma$ -electrons’. This label is used for diagnostic purposes only and remains with the electron until it is absorbed at one of the electrodes.

An electron arriving at an electrode can be elastically reflected, or inelastically reflected (re-emitted), can cause SEE, or can be absorbed (sticking). The probability of each of these surface processes is given by the actual impact energy ( $\varepsilon$ ) and angle of incidence ( $\theta$ ) dependent yield functions, which are collected in coherent sets for each electrode material individually. These yields are referred to as  $\eta_e(\varepsilon, \theta)$  for elastic reflection,  $\eta_i(\varepsilon, \theta)$  for inelastic reflection (where the electron is reflected with random direction and random energy between 0 and the impact energy from the surface), and  $\delta(\varepsilon, \theta)$  for SEE (where the impacting electron is lost, but it does induce the emission of one or more secondary electrons with random direction and random kinetic energy between 0 and 20 eV from the surface, in agreement with general trends observed for different materials [74]), and the sticking coefficient  $s(\varepsilon, \theta) = 1 - \eta_e - \eta_i$  for absorption. We adopt the phenomenological model for the yield functions as it was proposed in [75] based on [76, 77] and discussed in [33, 34] for  $\text{SiO}_2$  with model parameters listed in table 1 and shown in figure 2(b). For pure Si we apply the same surface model and perform adjustments to find the parameters that reproduce experimental [78–80] and numerical [81] data, resulting in the values listed in table 1 and shown in figure 2(c). Electrons that are emitted from the surface by electron induced secondary emission are labeled ‘ $\delta$ -electrons’. This label is used for

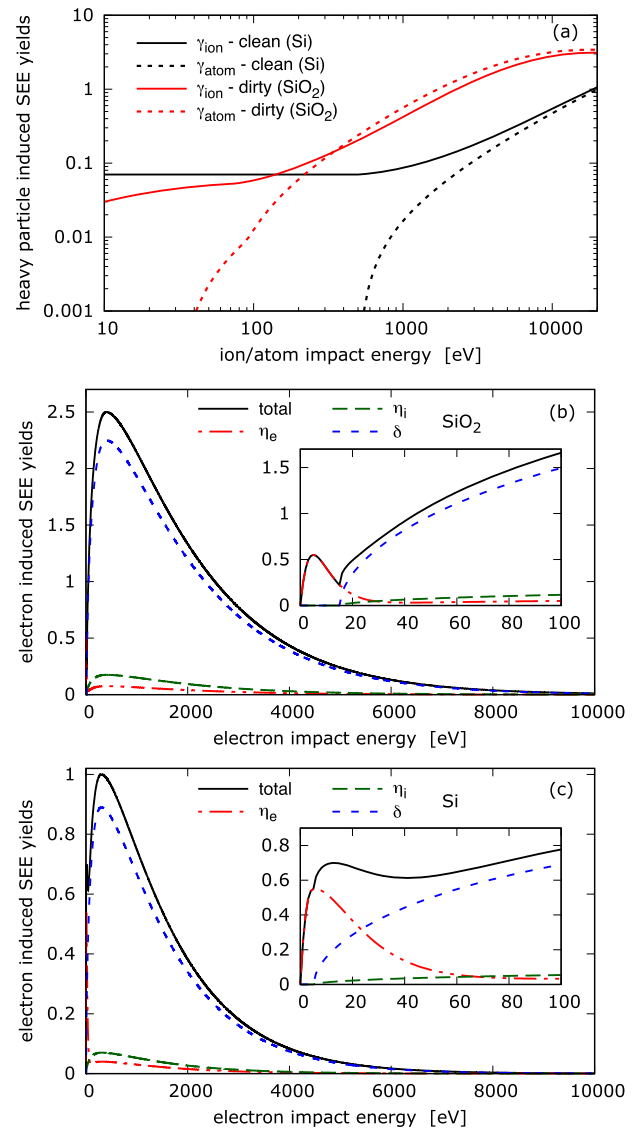


**Figure 2.** Impact energy dependent yields of surface processes: (a) heavy particle ( $\text{Ar}^+$  and  $\text{Ar}^f$ ) induced secondary electron emission (SEE) for ‘clean’ and ‘dirty’ metals [73]; (b) electron induced electron emission processes (elastic/inelastic reflection, SEE) for  $\text{SiO}_2$  surface [33], and (c) for pure Si surface.

diagnostic purposes only and remains with the electron until it is absorbed at one of the electrodes.

In case of electric charges being absorbed by or emitted from the powered electrode, its total (time-averaged) charge state, and with this its electric potential (relative to the ideally grounded counter-electrode), referred to as DC self-bias  $V_{\text{DC}}$  becomes shifted. In the simulation this is taken into account by counting the net influx of charges to the powered electrode over the time of one low-frequency period  $T_{\text{lf}}$  and adjusting  $V_{\text{DC}}$  after each cycle assuming a constant capacitance value for the electrode,  $C = 10$  pF for  $1 \text{ cm}^2$  electrode area in our case.

## 2.3. Electric field and temperature calculation

Besides the use of super-particles that represent a high number of real ones, the assumption that charged particles do not

**Table 1.** Parameters of the complex model of the electron-surface processes for SiO<sub>2</sub> and Si as described in detail in [33]. SEE = secondary electron emission, PE = primary (impacting) electron.

Parameter	Description	SiO <sub>2</sub>	Si
$\varepsilon_0$	The threshold energy for electron induced SEE	15 eV	5 eV
$\varepsilon_{\max,0}$	The energy of PE at the maximum emission	400 eV	300 eV
$\sigma_{\max,0}$	The maximum emission at normal incidence	2.5	1.0
$k_s$	Smoothness factor of the surface	1	1.5
$\varepsilon_{e,0}$	The threshold energy for elastic reflection	0 eV	0 eV
$\varepsilon_{e,\max}$	The energy of PE at the maximum elastic reflection	5 eV	5 eV
$\eta_{e,\max}$	The maximum of the elastic reflection	0.55	0.55
$\Delta_{e,\max}$	Control parameter for the decay of $\eta_e$	5	12
$r_e$	Portion of elastically reflected electrons at high energies	0.03	0.04
$r_i$	Portion of inelastically reflected electrons at high energies	0.07	0.07

interact with each other in form of binary collisions, but only through the self-consistent electric field determined by the boundary conditions and the momentary density distribution of electric charges in the discharge gap, is the second major approximation the PIC method is built on. This is expressed by Poisson's equation for the electric potential  $\Phi$  in every time-step in form of

$$\frac{d^2\Phi(x)}{dx^2} = e \frac{n_e(x) - n_i(x)}{\varepsilon_0}, \quad (3)$$

where  $n_e$  and  $n_i$  are the number densities of electrons and single charged Ar<sup>+</sup> ions, respectively,  $e$  is the elementary charge, and  $\varepsilon_0$  is the permittivity of free space.

To solve equation (3), one needs to discretize space by introducing a numerical grid and define the boundary conditions. We apply the finite-difference method and define a one-dimensional (1D) equidistant mesh along the  $x$ -axis with grid spacing  $\Delta x$ . Similar to the time-step  $\Delta t$ , there are stability and accuracy criteria for the choice of  $\Delta x$  that have to be considered during the implementation. The numerical grid has to resolve all relevant length-scales in the plasma, such as the Debye-length,  $\lambda_D$ , i.e.  $\Delta x < \lambda_D$ . Another criterion relates the total number of super-particles and the grid spacing, by requiring at least a few hundred particles per grid cell on average. Otherwise artificial density fluctuations originating from the weak statistics may cause false fluctuations of the electric field and thus non-realistic electron heating [82]. In the present study, 1024 grid points are used within the electrode gap of  $L = 5$  cm. The boundary conditions are defined as:

$$\begin{aligned} \Phi(0, t) &= V_{\text{lf}} \cos(2\pi f_{\text{lf}}t) + V_{\text{hf}} \cos(2\pi f_{\text{hf}}t) + V_{\text{DC}}, \\ \Phi(L, t) &\equiv 0, \end{aligned} \quad (4)$$

where  $V$  and  $f$  are the voltage amplitudes and frequencies of the low-frequency (lf) and high-frequency (hf) components, respectively. To assign the momentary positions of the  $10^5$  to  $10^6$  particles in the simulation to the numerical grid and construct  $n_e(x)$  and  $n_i(x)$  distributions, we apply a simple linear shape function that distributes the contribution of every particle to the two grid points directly bracketing its position. We apply the intrinsically serial Thomas algorithm [83] to solve equation (3) on the CPU. All other computations

are performed on the GPU device. The electric field  $E(x, T)$  needed for the particle pusher is simply calculated by  $E = -d\Phi/dx$  and later interpolated from the grid to the actual positions of the particles.

The gas heating calculation is adopted from reference [57]. Similarly to the density distributions  $n_e(x)$  and  $n_i(x)$ , the gas heating power per unit volume  $S(x)$  is constructed from individual collision events, as described in section 2.1.3, and assigned to the numerical grid based on the same method. To compute the gas temperature we seek for the equilibrium solution of the heat transport equation in the form

$$\frac{d^2 T}{dx^2} = -\frac{S(x)}{\kappa}, \quad (5)$$

where  $\kappa = 0.001165 + 6.255 \times 10^{-5}T - 2.25 \times 10^{-8}T^2$  is the thermal conductivity of argon in units of  $\text{Wm}^{-1}\text{K}^{-1}$  [84]. The electrodes (walls) have a constant temperature of  $T_w = 400$  K, and the boundary conditions for equation (5) include a temperature jump at the electrodes caused by the low operating pressure and temperature gradients near the surfaces. The solution for  $T(x)$  is found by iterating the tri-diagonal solver (same as for Poisson's equation) and adjusting the gas temperature at the walls  $T_g = T_w + \lambda(dT/dx)_{\text{wall}}$ , as discussed in references [57, 85, 86].

#### 2.4. Implementation and performance

It has been realized already at the planning phase of these studies, that very short time-steps are needed to fulfill the Courant stability condition at these high voltages. At the same time, the limits for the spatial grid resolution and the number of super-particles necessary are set by the Debye-length and particle statistics. With our existing serial CPU based simulations the estimated execution time needed to reach convergence was in the range of 8 to 10 weeks for each case (e.g. on an Intel Xeon Gold 6132 server). This made parallelization of the code necessary. Following preliminary studies we have chosen to utilize GPUs and the NVIDIA CUDA programming language extension. In our case each particle is assigned to an individual parallel computation thread and all PIC/MCC steps (except for the Poisson solver) and diagnostic routines are

executed in parallel on the GPU. With this new GPU implementation the simulation time could be reduced to about 1 day/case on an NVIDIA P100 device, with super-particle numbers in the range of  $10^5 < N < 5 \times 10^5$ . This represents a speedup factor of about 60 with respect to the CPU code.

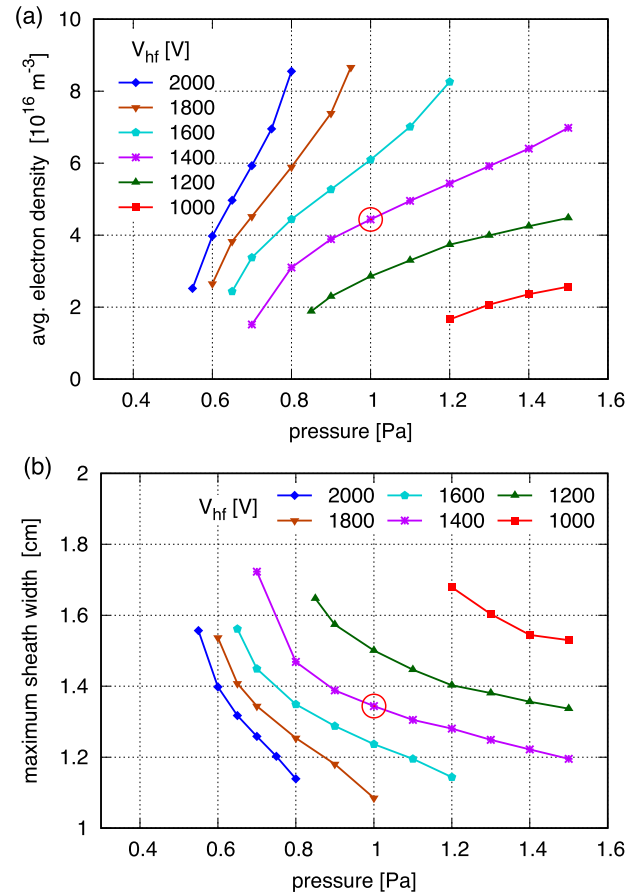
### 3. Results

Our 1D electrostatic PIC/MCC simulation is applied to cases where the driving voltage waveform is a combination of a  $f_{lf} = 400$  kHz low-frequency component with constant  $V_{lf} = 10$  kV amplitude and a  $f_{hf} = 40$  MHz high-frequency component with a voltage amplitude that is varied in the range of  $1000 \text{ V} \leq V_{hf} \leq 2400 \text{ V}$ , see equation (4). The argon gas pressure is set within the range of  $0.5 \text{ Pa} \leq p \leq 1.5 \text{ Pa}$ . The two types of electrode materials considered in the simulations are  $\text{SiO}_2$  and pure Si, which are studied in symmetric (identical surface materials for both electrodes) and asymmetric (different surface materials at both electrodes) configurations. The discharge gap between the plane-parallel electrodes is  $L = 5 \text{ cm}$ .

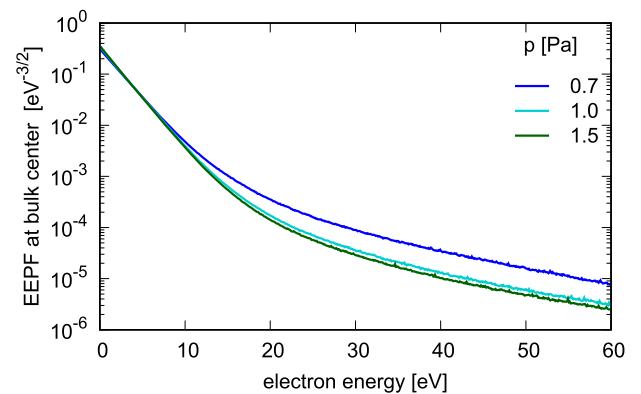
#### 3.1. Dual-frequency CCP with identical electrode materials

Figure 3(a) shows the space and time averaged electron density as a function of the pressure and the high-frequency driving voltage amplitude in the dual-frequency CCP operated at  $f_{lf} = 400$  kHz and  $f_{hf} = 40$  MHz at a fixed  $V_{lf} = 10$  kV and an electrode gap of 5 cm. For both electrodes the  $\text{SiO}_2$  surface model is applied. Due to the symmetry of both the electrode configuration and the driving voltage waveform the DC self-bias voltage has to be zero and this is indeed confirmed by the self-consistent calculation included in the simulation. The results show an increase of the plasma density as a function of  $p$  and  $V_{hf}$ . This trend appears equally in the total ionization rate data (not shown here). The increase as a function of the hf driving voltage amplitude is caused by an enhancement of the power dissipation to electrons via the spatio-temporal electron dynamics discussed for an exemplary case in detail below. The drastic decay of the plasma density towards lower pressures is caused by a strong increase of the sheath widths adjacent to both electrodes, as shown in figure 3(b) for the same conditions. This, in turn, is caused by an increase of the electron mean free path and a more pronounced decrease of the ion density towards the adjacent electrode due to ion flux continuity in collisionless sheaths at low compared to high pressures. At low pressures, the long electron mean free path leads to an inefficient energy relaxation of electrons in the discharge, i.e. energetic electrons propagate collisionlessly through the electrode gap and impact at boundary surfaces, where they are lost with a high probability. Thus, the plasma density is decreased and for a given driving voltage the sheath widths are increased.

Figure 4 shows the time averaged electron energy probability function (EPPF) collected from a 1 mm narrow region centered at the density peak position in the plasma bulk for three selected pressures. The EPPFs follow bi-Maxwellian distributions, frequently reported in CCPs [18]. The relative depopulation of the high energy tail with increasing pressure



**Figure 3.** Spatio-temporally averaged electron density (a) and maximum sheath width (b) as a function of the pressure ( $p$ ) and the high-frequency driving voltage amplitude ( $V_{hf}$ ) in the CCP with identical surface materials at both electrodes ( $\text{SiO}_2$ ). The red circle indicates the discharge conditions that are analyzed in detail.  $L = 5 \text{ cm}$ ,  $f_{lf} = 400 \text{ kHz}$ ,  $f_{hf} = 40 \text{ MHz}$  and  $V_{lf} = 10 \text{ kV}$ .



**Figure 4.** Time averaged electron energy probability function EPPF in the center of the bulk region in the CCP with identical surface materials ( $\text{SiO}_2$ ) at both electrodes at  $p = 0.7, 1.0$ , and  $1.5 \text{ Pa}$ , and  $V_{hf} = 1400 \text{ V}$ .  $L = 5 \text{ cm}$ ,  $f_{lf} = 400 \text{ kHz}$ ,  $f_{hf} = 40 \text{ MHz}$  and  $V_{lf} = 10 \text{ kV}$ .

is observed, while the transition between the low and high energy populations happens in the 15–20 eV energy range, significantly higher than in dual frequency Ar discharges operating at lower voltages and higher pressures [18].

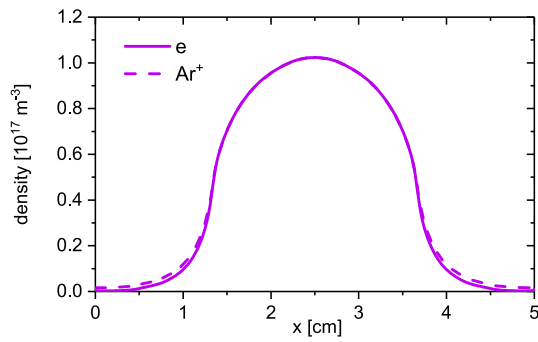


**Figure 5.** Time averaged electron and ion density in the CCP with identical surface materials ( $\text{SiO}_2$ ) at both electrodes at  $p = 1$  Pa and  $V_{\text{hf}} = 1400$  V.  $L = 5$  cm,  $f_{\text{lf}} = 400$  kHz,  $f_{\text{hf}} = 40$  MHz and  $V_{\text{lf}} = 10$  kV.

For plasma etching the low-frequency driving voltage amplitude needs to be high to realize high ion bombardment energies at the wafer, that are sufficient to overcome repelling electric fields inside HAR trenches generated by positive wall charges inside these features. At the same time the sheath width needs to be small enough to ensure collisionless conditions near the wafer to ensure high ion bombardment energies [2]. Moreover, a high plasma density and ion flux are required to realize high process rates.

In order to understand the operation of a CCP under the conditions of a low pressure, very low  $f_{\text{lf}}$ , and very high  $V_{\text{lf}}$ , we analyze the spatio-temporal ionization dynamics as well as the formation of charged particle flux-energy/velocity distribution functions at the boundary surfaces in detail for one exemplary case indicated by the red circle in figure 3:  $p = 1$  Pa,  $V_{\text{hf}} = 1400$  V. Clearly, in order to optimize a distinct etch process specific investigations under the exact discharge conditions of this process are required in terms of e.g. gas mixture and reactor geometry. However, this is not the scope of this work.

Figure 5 shows the time averaged electron and ion density profiles for the exemplary case, for which a well-pronounced quasineutral plasma bulk region is generated. Due to the application of very high lf and hf driving voltage amplitudes and based on the ionization dynamics described in detail below, a high plasma density with a maximum value of about  $1 \times 10^{17} \text{ m}^{-3}$  at the discharge centre is obtained.

Figure 6 shows the spatio-temporal distribution of the electric field for the same conditions. The field is high in and close to the sheath regions at both electrodes, and essentially zero inside the quasineutral bulk. Due to the high plasma density the maximum sheath width is restricted to about 1.4 cm at each electrode. The sheaths oscillate  $180^\circ$  out of phase at each electrode and the sheath width is affected by both the low and high-frequency driving voltage waveforms. As the high-frequency of 40 MHz is 100 times higher than the low-frequency of 400 kHz, there are 100 high-frequency periods within each low-frequency period. Clearly, the instantaneous lf voltage affects the hf sheath oscillation. For instance, when the applied lf voltage is close to its maximum around  $t = 0$ , at the powered electrode the sheath oscillates in direct vicinity of the electrode in a region of low ion density, whereas

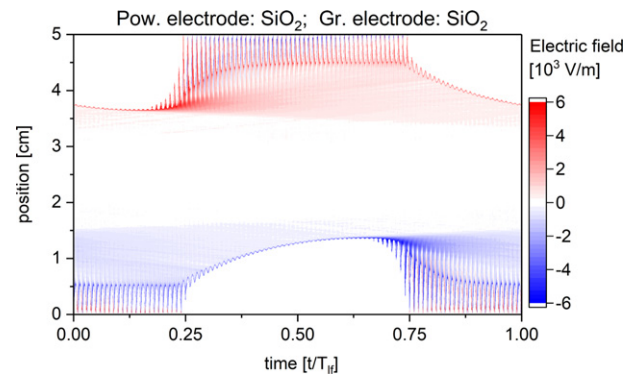


**Figure 6.** Spatio-temporal plot of the electric field in the CCP with identical surface materials ( $\text{SiO}_2$ ) at both electrodes at  $p = 1$  Pa and  $V_{\text{hf}} = 1400$  V. The high electric fields within the sheaths are not shown.  $L = 5$  cm,  $f_{\text{lf}} = 400$  kHz,  $f_{\text{hf}} = 40$  MHz and  $V_{\text{lf}} = 10$  kV. The powered electrode is situated at  $x = 0$ , while the grounded electrode is at  $x = L$ . This is the same for all forthcoming figures of this style.

it oscillates far away from the adjacent electrode in a region of higher ion density at the grounded electrode at the same time within the lf period. For a given hf driving amplitude, this effect—known as frequency coupling [87]—leads to high sheath expansion velocities at the powered and to low sheath expansion velocities at the grounded electrode at this time within the lf period.

The results obtained with the implementation of a complex SEE model in the simulation show that a high number of secondary electrons is emitted at the electrodes as a consequence of high energy ion and electron bombardment. Under these discharge conditions the effective heavy particle induced SEE yield is  $\gamma_{\text{eff}} = (1/N_i) \cdot \left( \sum_{k=1}^{N_i} \gamma_i(\varepsilon_k) + \sum_{k=1}^{N_a} \gamma_a(\varepsilon_k) \right) = 2.0$ , where  $N_i$  and  $N_a$  are the total number of  $\text{Ar}^+$  ions and  $\text{Ar}^f$  atoms reaching the electrodes during a low-frequency period and  $\varepsilon_k$  is the energy of the  $k$ th ion or atom at arrival at the electrode. The effective electron induced SEE yield is  $\delta_{\text{eff}} = 1/N_e \cdot \sum_{k=1}^{N_e} \delta(\varepsilon_k) = 0.22$ , where  $N_e$  is the total number of electrons reaching the electrodes during one low-frequency period and  $\varepsilon_k$  is the energy of the  $k$ th electron at the electrode. Such a strong electron emission from boundary surfaces effectively reduces the electron flux to each electrode [35, 36]. In order to compensate the high ion flux to the electrode on time average in the presence of such strong electron emission [88], electric field reversals are generated at the times of sheath collapse at each electrode. Such reversed electric fields are visible as red regions at the powered electrode and as blue regions at the grounded electrode in figure 6. In this way, electrons are pulled towards the electrode during sheath collapse. As electrons are accelerated towards the electrode, they impinge at the surface at energies significantly above the thermal electron energy. While the probability for these electrons to be absorbed at the electrode is high, they will also cause the emission of  $\delta$ -electrons with an energy and material dependent probability according to figure 2. Ultimately, the reversed electric field is self-adjusted to ensure flux compensation at the electrode in the presence of such electron emission.

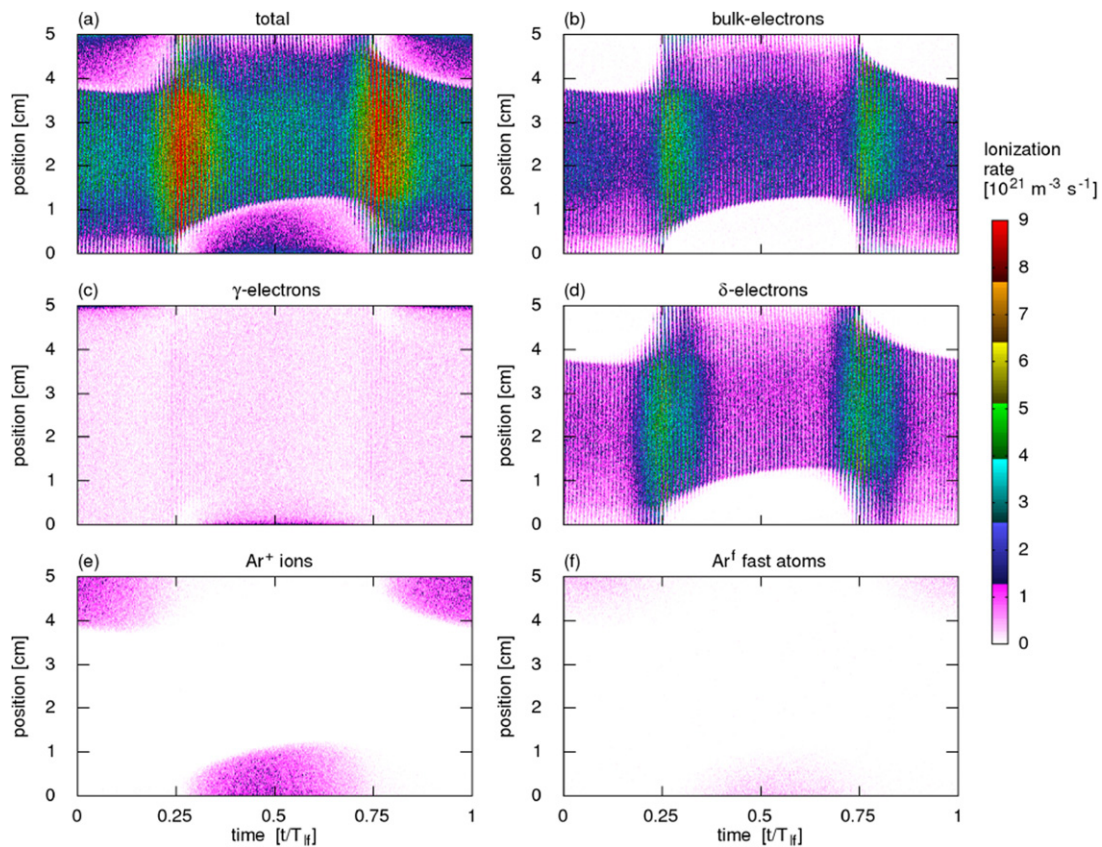


**Figure 7.** Spatio-temporal plots of the ionization rate generated by all particles (electrons, ions, fast neutrals) (a), bulk electrons (b),  $\gamma$ -electrons (c),  $\delta$ -electrons (d), ions (e), and fast atoms (f) in a dual-frequency CCP with identical surface materials ( $\text{SiO}_2$ ) at both electrodes at  $p = 1$  Pa and  $V_{\text{hf}} = 1400$  V.  $L = 5$  cm,  $f_{\text{lf}} = 400$  kHz,  $f_{\text{hf}} = 40$  MHz and  $V_{\text{lf}} = 10$  kV.

Finally, figure 6 shows significant electric fields outside the sheaths, that are time modulated within the low-frequency period. Based on previous work [89, 90], these electric fields are identified to be predominantly ambipolar electric fields.

Figure 7 shows the spatio-temporally resolved ionization rate caused by all particles (electrons, ions, fast neutrals) (a), bulk electrons (b), heavy particle induced  $\gamma$ -electrons (c), electron induced  $\delta$ -electrons (d), ions (e), and fast atoms (f) within one lf period under the chosen set of discharge conditions. The highest ionization rate is observed, when the low and high-frequency components of the driving voltage induce sheath expansion simultaneously, i.e. at about  $t/T_{\text{lf}} \approx 0.25$  and  $t/T_{\text{lf}} \approx 0.75$ . It is caused by electrons accelerated by the expanding sheath at times of high sheath expansion velocity, i.e. via sheath heating, and occurs at a time within the lf period, when the sheath edge oscillates in vicinity of the electrode, but not directly in front of it. At this position the ion density is higher compared to that near the electrode surface, i.e. more electrons are accelerated. At earlier times fewer electrons are accelerated and the constructive superposition of lf and hf sheath expansion is less pronounced. At later times the sheath edge oscillates further away from the electrode in a region of higher ion density, so that the sheath expansion velocity is low. At the low pressure non-local discharge conditions studied here, electrons accelerated by the expanding sheath in this way can cause ionization everywhere in the plasma bulk due to the long electron mean free path.

In contrast to previous simulations of low pressure CCPs operated at lower voltages, which do not include a realistic description of SEE [29, 91], we find that a significant fraction, about 41%, of the total ionization, is caused by electron induced  $\delta$ -electrons (see figure 7(d)) and only 48% is caused by bulk electrons, for the given conditions. As a consequence of the ionization caused by these  $\delta$ -electrons new bulk electrons are generated, which can again cause ionization, but would not exist, if  $\delta$ -electrons were not included in the simulation. This means that neglecting electron induced SEE under such discharge conditions results in an unrealistic description of the discharge.

Figure 8(a) shows the current density of  $\delta$ -electrons emitted at the grounded electrode as a function of time within one lf period. No time resolution within the hf periods is provided in this plot, i.e. the data are averaged over the duration of one hf period. This hf time resolution is provided in figure 8(b) for three exemplary consecutive hf periods together with the spatio-temporal dynamics of the electric field in the sheath region at the grounded electrode. In figures 8(a) and (b) the outgoing current density of  $\delta$ -electrons is separated into different groups according to the types of electrons that cause their emission at the electrode, i.e. into  $\delta$ -electrons generated by bulk electrons, by  $\delta$ -electrons originally generated at the powered and grounded electrode, as well as by  $\gamma$ -electrons originally generated at the powered and grounded electrode. Similar phenomena are observed at the powered electrode half

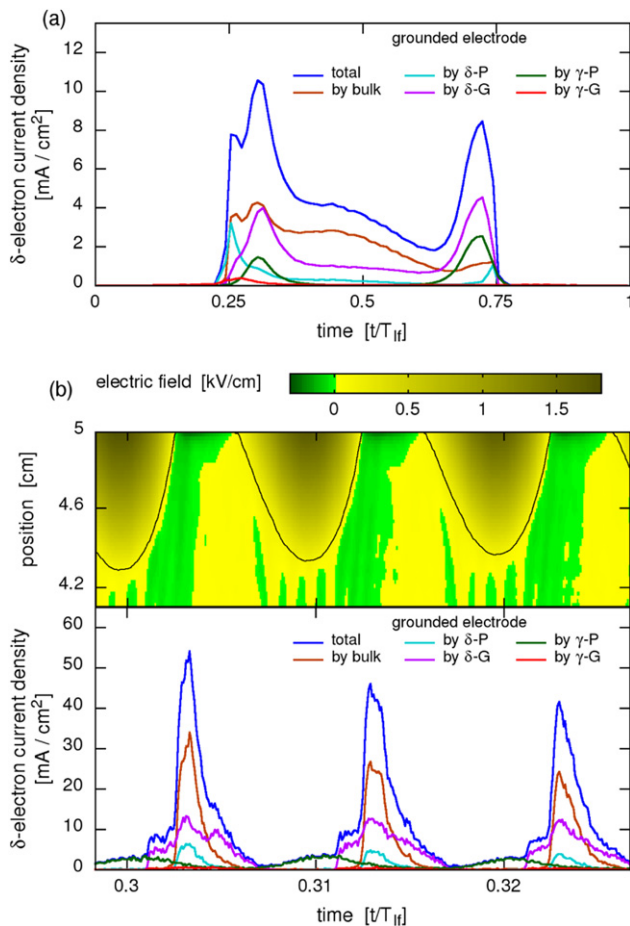


**Figure 8.** Current density of emitted  $\delta$ -electrons at the grounded electrode as a function of time within one  $1f$  period without temporal resolution within the hf period (a) and with temporal resolution within the hf period for three selected hf periods including the spatio-temporal dynamics of the electric field adjacent to the grounded electrode (b). The lines indicate the contribution of different groups of electrons to the generation of  $\delta$ -electrons at this electrode, i.e. the contributions of bulk,  $\delta$ -, and  $\gamma$ -electrons emitted from the powered (P) and grounded (G) electrodes. Discharge conditions:  $p = 1$  Pa,  $L = 5$  cm,  $f_{lf} = 400$  kHz and  $f_{hf} = 40$  MHz,  $V_{lf} = 10$  kV and  $V_{hf} = 1400$  V, identical electrode surface materials ( $\text{SiO}_2$ ).

a  $1f$  period later. At the grounded electrode  $\delta$ -electrons are generated during the phase of  $1f$  sheath collapse, i.e. at  $0.25 \leq t/T_{lf} \leq 0.75$  (see also figure 6), when the local sheath voltage is low and electrons can reach the electrode. Except for the very highly energetic  $\gamma$ -electrons generated at the powered electrode, figure 8(b) shows that  $\delta$ -electrons are generated at the grounded electrode, when the  $1f$  and hf component of the local sheath are collapsed simultaneously.

Most  $\delta$ -electrons are generated by energetic bulk electrons, whose energy is above the threshold of  $\delta$ -electron emission for  $\text{SiO}_2$  (see figure 2). Figure 8(b) shows that these bulk electrons are accelerated to these sufficiently high energies by the electric field reversals during the hf sheath collapse. These regions are indicated by the green color in the spatio-temporal electric field plot in figure 8(b) and are generated due to the presence of strongly emitting boundary surfaces [35, 36]. The strong electron emission from boundary surfaces, in turn, is mostly

caused by the very high effective heavy particle induced SEEC of  $\gamma_{\text{eff}} \approx 2$  due to the very high ion bombardment energies as a consequence of the high  $1f$  driving voltage amplitude and the low neutral gas pressure. The temporal modulation of the outgoing flux of  $\delta$ -electrons shown in figure 8(a) correlates with the temporal modulation of the reversed electric field at the grounded electrode (see figure 6).

The second strongest contribution to the  $\delta$ -electron emission from the grounded electrode is made by  $\delta$ -electrons emitted from this electrode themselves. Such electrons propagate through the plasma bulk, are reflected at the sheath adjacent to the powered electrode, which is expanded for  $0.25 \leq t/T_{lf} \leq 0.75$ , and hit the grounded electrode, where, depending on their energy, they can cause  $\delta$ -electron emission. According to figure 8(a) maximum  $\delta$ -electron emission due to this group of electrons is caused shortly after  $t/T_{lf} = 0.25$  and shortly before  $t/T_{lf} = 0.75$ , i.e. during the phase of  $1f$  sheath collapse and expansion at this electrode. This is caused by the fact that  $\gamma$ -electrons generated at the powered electrode arrive at the grounded electrode with energies that are low enough to generate  $\delta$ -electrons at these times. According to figure 2(c),  $\gamma$ -electrons generated at the powered electrode during the time of full local sheath expansion will gain about 10 keV energy and will not be able to cause  $\delta$ -electron emission upon impact at the grounded electrode, since they are too energetic. Only during the phase of sheath expansion and collapse at the powered electrode  $\gamma$ -electrons with appropriate energies are generated, since the instantaneous local sheath voltage is lower. Such  $\gamma$ -electrons will still be too energetic to cause  $\delta$ -electron emission at the grounded electrode, if they impact at the time of local sheath collapse at the grounded electrode. Figure 8(b) shows, that they will only generate  $\delta$ -electrons at the grounded electrode, if they arrive there at the time of high instantaneous hf sheath voltage, since in this case they will be decelerated by the instantaneous local sheath electric field to low enough energies that allow them to generate  $\delta$ -electrons at the grounded electrode. For this reason  $\delta$ -electrons generated in this way always appear earlier compared to those generated by other groups of electrons, which can only reach the electrode during the local sheath collapse. In between  $t/T_{lf} = 0.25$  and  $t/T_{lf} = 0.75$ ,  $\gamma$ -electrons from the powered electrode do not generate  $\delta$ -electrons efficiently at the grounded electrode, because they are accelerated to too high energies at the powered electrode and are too energetic upon impact. Thus, the creation of  $\delta$ -electrons at the grounded electrode by  $\delta$ -electrons from this electrode is also low during this time window. The contribution of  $\delta$ -electrons created at the powered electrode to the generation of electron induced secondary electrons at the grounded electrode is only high at the beginning and end of this time window, since at these times a high number of energetic  $\delta$ -electrons is generated at the powered electrode via the mechanisms described above and can hit the grounded electrode at adequate energies. The contribution of  $\gamma$ -electrons created at the grounded electrode to the local generation of  $\delta$ -electrons is always low, since at the times of high sheath voltage at the grounded electrode within one  $1f$  period such electrons will be absorbed at the powered electrode, where the sheath voltage is low at these times, and

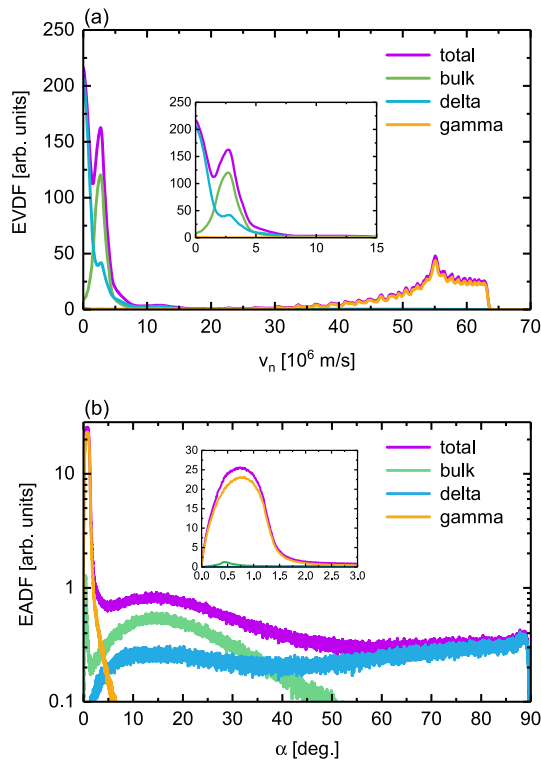


**Figure 9.** Electron velocity distribution (as a function of the velocity component normal to the surface) (a) and angular distribution (as a function of the angle relative to the surface normal) (b) at the electrodes for all electrons (total), bulk electrons,  $\delta$ -electrons, and  $\gamma$ -electrons in a dual-frequency CCP with identical surface materials ( $\text{SiO}_2$ ) at both electrodes at  $p = 1$  Pa and  $V_{\text{hf}} = 1400$  V.  $L = 5$  cm,  $f_{\text{lf}} = 400$  kHz,  $f_{\text{hf}} = 40$  MHz and  $V_{\text{lf}} = 10$  kV.

at the times, when the sheath voltage at the powered electrode is high enough to reflect such  $\gamma$ -electrons back towards the grounded electrode, only a few energetic  $\gamma$ -electrons are generated at the grounded electrode, since the local sheath voltage is low at these times within the 1f period.

Ionization by  $\gamma$ -electrons is only observed in the direct vicinity of the electrodes at times of high local sheath voltage (see figure 7(c)). The reason for this is that these electrons are rapidly accelerated to very high energies by the sheath electric field, at which the cross-section for ionization has decayed significantly from its maximum, that occurs at about 100 eV. Therefore, the contribution of  $\gamma$ -electrons to the total ionization is only 7%.

Figures 7(e) and (f) show weak contributions of ions and fast neutrals to the ionization inside the sheaths, where these heavy particles have sufficient energy to ionize. Electrons generated by heavy particle induced ionization are considered to be bulk electrons in the simulation. As these electrons are created inside the sheaths, they are accelerated to high energies. Their contributions to the  $\delta$ -electron generation upon impact at the opposite electrode is, however, below 6% of the contribution of bulk electrons and is, therefore, not shown separately in figure 8. The contribution of heavy particle induced ionization to the total ionization is 4%.

These findings show that extremely high driving voltages at low pressures and low driving frequencies result in

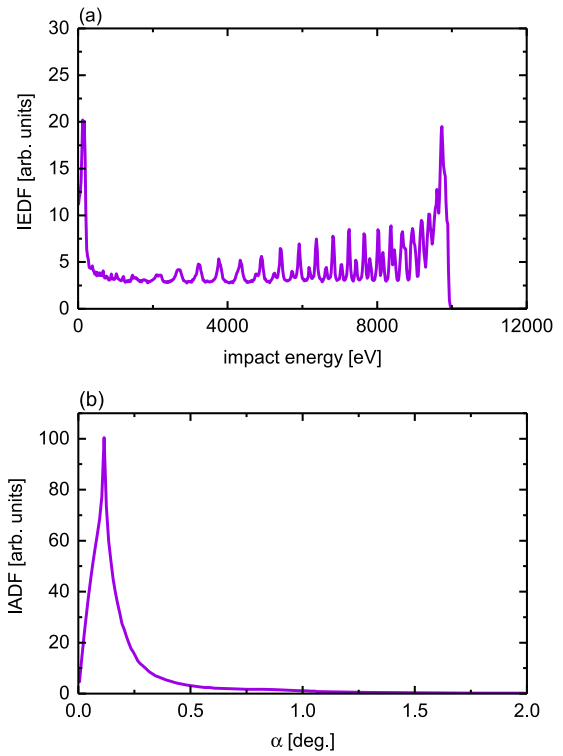


**Figure 10.** Ion energy distribution (a) and angular distribution (as a function of the angle relative to the surface normal) (b) at the electrodes in a dual-frequency CCP with identical surface materials ( $\text{SiO}_2$ ) at both electrodes at  $p = 1$  Pa and  $V_{\text{hf}} = 1400$  V.  $L = 5$  cm,  $f_{\text{lf}} = 400$  kHz,  $f_{\text{hf}} = 40$  MHz and  $V_{\text{lf}} = 10$  kV.

ionization dynamics, which are very different from classical CCPs, where  $\delta$ -electrons are typically considered to be irrelevant and  $\gamma$ -electrons are assumed to play an important role only at higher pressures, where their collisional multiplication inside the sheaths can form electron avalanches that induce ionization maxima at the position of maximum sheath width and at the times of maximum sheath voltage within the RF period ( $\gamma$ -mode).

In the following, we turn to the analysis of the velocity, energy, and angular distributions of the charged particles at the electrode surfaces. The distribution functions displayed are constructed by counting the number of particles within bins with certain widths in energy, velocity, or angle. Thus, these are related to the flux of the particles arriving at given energies, velocities, or at given angles of incidence. We note that the angular distribution functions obtained in this way differ from those that are defined in the volume, by a factor of  $\sin(\alpha)$ , where  $\alpha$  is the angle of incidence relative to the surface normal. Results in the literature can be found for both definitions, see e.g. [7, 92–94]. Our choice is motivated by the fact that for etching the number of particles incident to a trench orifice at a given angle matters.

Figure 9(a) shows the time averaged electron velocity distribution function (EVDF) at the electrodes as a function of the velocity component normal to the surface,  $v_n$ , split into the different groups of electrons, i.e. bulk-,  $\delta$ - and  $\gamma$ -electrons. A large number of bulk- and  $\delta$ -electrons reaches the electrodes at low velocities during sheath collapse (see also the inset plot in

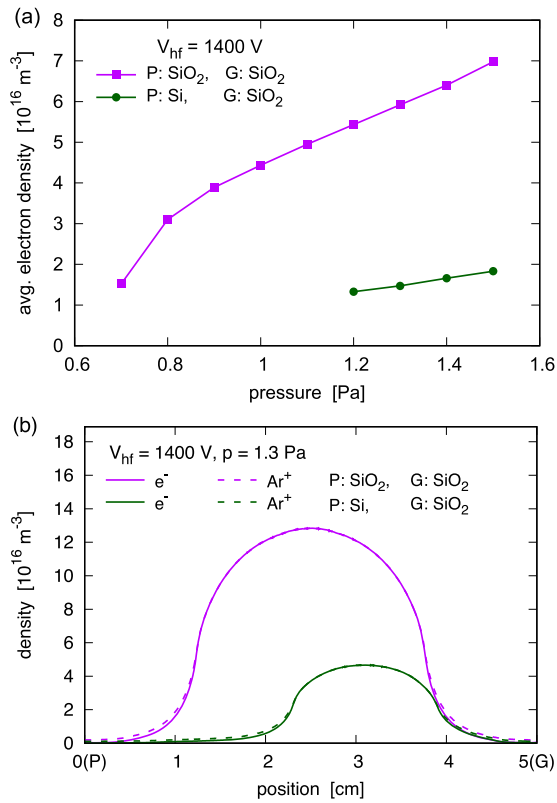


**Figure 11.** Spatio-temporally averaged electron densities as a function of the pressure in a dual-frequency CCP, where (i) the powered (P) as well as the grounded (G) electrode are both made of  $\text{SiO}_2$  and (ii) where the powered electrode is made of Si, whereas the grounded electrode is made of  $\text{SiO}_2$  (a). Axial profiles of the electron density for these two scenarios at  $p = 1.3 \text{ Pa}$  (b).  $L = 5 \text{ cm}$ ,  $f_{\text{lf}} = 400 \text{ kHz}$ ,  $f_{\text{hf}} = 40 \text{ MHz}$ ,  $V_{\text{lf}} = 10 \text{ kV}$  and  $V_{\text{hf}} = 1400 \text{ V}$ . In the legends  $\text{SiO}_2/\text{Si}$  indicates the surface model used.

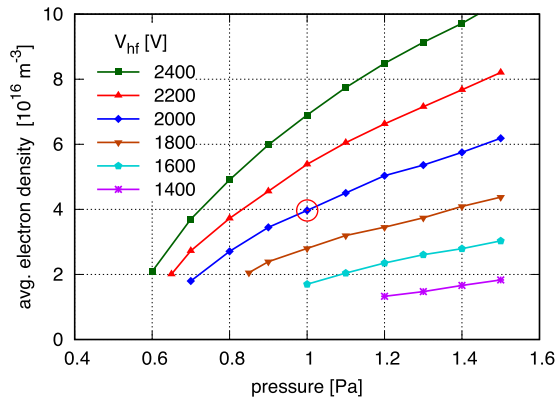


**Figure 12.** Spatio-temporally averaged electron densities as a function of pressure and high-frequency voltage amplitude in dual-frequency CCPs with a Si surface at the powered electrode and a  $\text{SiO}_2$  surface at the grounded electrode. The red circle indicates the discharge conditions that are analyzed in detail.  $L = 5 \text{ cm}$ ,  $f_{\text{lf}} = 400 \text{ kHz}$ ,  $f_{\text{hf}} = 40 \text{ MHz}$  and  $V_{\text{lf}} = 10 \text{ kV}$ .

figure 9(a)). These low velocity electrons are divided into two groups corresponding to the two peaks of the EVDF observed at low values of  $v_n$ . The peak at the lowest velocity mostly corresponds to  $\delta$ -electrons, while the second peak at higher velocities corresponds to more energetic bulk electrons arriving at

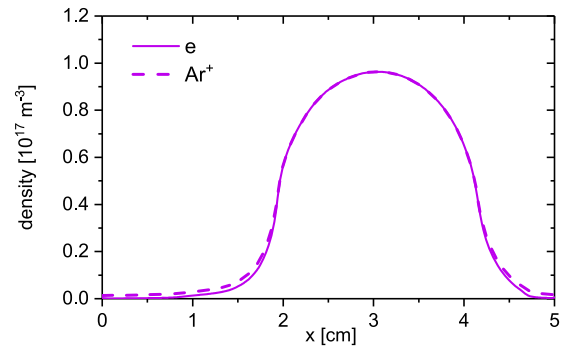


**Figure 13.** Axial profile of the time averaged electron and ion density in a dual-frequency CCPs with a Si surface at the powered electrode and a  $\text{SiO}_2$  surface at the grounded electrode at  $p = 1 \text{ Pa}$  and  $V_{\text{hf}} = 2000 \text{ V}$ .  $L = 5 \text{ cm}$ ,  $f_{\text{lf}} = 400 \text{ kHz}$ ,  $f_{\text{hf}} = 40 \text{ MHz}$  and  $V_{\text{lf}} = 10 \text{ kV}$ .

the electrode as a consequence of electron acceleration by the reversed electric field. Heavy particle induced  $\gamma$ -electrons generated and accelerated to very high velocities by the sheath electric field at the opposite electrode arrive at much higher values of  $v_n$ . Their velocity distribution is broad as a consequence of the temporal modulation of the sheath voltage at the opposite electrode within the lf period.

The electron angular distribution function (EADF) at the electrode is shown in figure 9(b). From the figure we can see that the EADF is relatively broad with a peak at small angles relative to the surface normal due to energetic  $\gamma$ -electrons, while all electrons that arrive at the electrode at low velocities impinge under larger angles, because their velocity component parallel to the electrode surface is comparable to  $v_n$ .

The energy and angular distribution functions of the ions at the electrodes are shown in figure 10. Due to the high driving voltage amplitudes, extremely energetic (up to 10 keV) and nearly vertical ion bombardment is realized at the electrodes. The ion energy distribution function (IEDF) shows a complex shape characterized by multiple peaks, which are not the consequence of collisions of ions inside the sheath at this low pressure, but appear because of the hf sheath voltage modulation superimposed on the lf sheath oscillation. The most prominent peaks appear close to 0 eV and close to the maximum ion energy of about 10 keV. These peaks correspond to a bi-modal ‘envelope’ caused by the low driving frequency of 400 kHz, to which the ions can react well.

### 3.2. Influence of the electrode materials

In this section, we investigate the effects of changing the surface material of the powered electrode to a different material (Si), while the grounded electrode remains to be made of  $\text{SiO}_2$ . In this sense a surface material asymmetry is introduced to the simulation. Figure 11(a) shows the spatio-temporally averaged electron density as a function of the neutral gas pressure for both scenarios, i.e. identical electrode materials ( $\text{SiO}_2$ ) and different electrode materials (Si at the powered and  $\text{SiO}_2$  at the grounded electrode). All other discharge conditions are identical to the scenario analyzed in detail in the previous section ( $L = 5 \text{ cm}$ ,  $f_{\text{lf}} = 400 \text{ kHz}$ ,  $f_{\text{hf}} = 40 \text{ MHz}$ ,  $V_{\text{lf}} = 10 \text{ kV}$  and  $V_{\text{hf}} = 1400 \text{ V}$ ). Similar to the results discussed in the

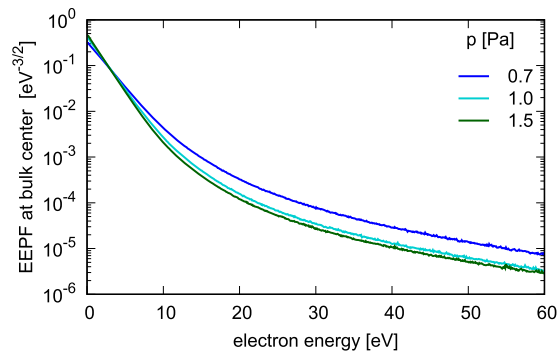


**Figure 14.** Time averaged electron energy probability function (EEPF) in the center of the bulk region in the CCP with a Si surface at the powered electrode and a SiO<sub>2</sub> surface at the grounded electrode at  $p = 0.7, 1.0,$  and  $1.5$  Pa, and  $V_{\text{hf}} = 2000$  V.  $L = 5$  cm,  $f_{\text{lf}} = 400$  kHz,  $f_{\text{hf}} = 40$  MHz and  $V_{\text{lf}} = 10$  kV.

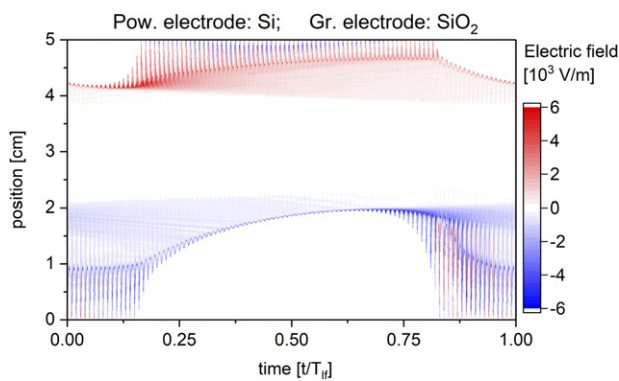


**Figure 15.** Spatio-temporal plot of the electric field in a dual-frequency CCP with a Si surface at the powered electrode and a SiO<sub>2</sub> surface at the grounded electrode at  $p = 1$  Pa and  $V_{\text{hf}} = 2000$  V. The high electric fields within the sheaths are not shown.  $L = 5$  cm,  $f_{\text{lf}} = 400$  kHz,  $f_{\text{hf}} = 40$  MHz and  $V_{\text{lf}} = 10$  kV.

previous section we find that the plasma density increases as a function of the neutral gas pressure in both cases. Moreover, the plasma density is strongly affected by the choice of the surface materials. Changing the surface material of the powered electrode from SiO<sub>2</sub> to Si causes a drastic decrease of the plasma density at all neutral gas pressures. In fact, the discharge can only be sustained at higher neutral gas pressures, if Si is used as the surface material of the powered electrode. This is caused by the difference of the SEECs due to heavy particle and electron impact between SiO<sub>2</sub> and Si (see figure 2). The heavy particle induced SEEC is significantly lower for Si compared to SiO<sub>2</sub> at high heavy particle incident energies and the electron induced SEEC is lower for Si, too. Therefore, less secondary electrons are emitted from the Si electrode and, thus, the ionization and finally the plasma density are reduced, especially in vicinity of that electrode. A specific example which illustrates this effect of the surface material on the plasma density is provided in figure 11(b), which shows the axial profile of the electron and ion density for these two scenarios at 1.3 Pa. If Si is used as the powered electrode surface instead of SiO<sub>2</sub>, the plasma density maximum decreases from  $13 \times 10^{16} \text{ m}^{-3}$  to  $4.7 \times 10^{16} \text{ m}^{-3}$  and shifts towards the SiO<sub>2</sub> electrode, where the SEECs are higher, i.e. a plasma

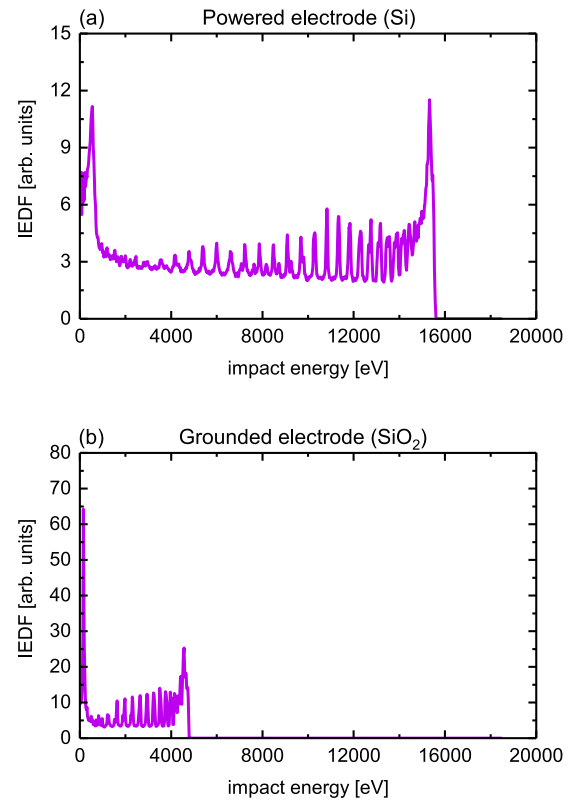


**Figure 16.** Ion energy distribution at the powered electrode (a) and at the grounded electrode (b) in a dual-frequency CCP with a Si surface at the powered electrode and a SiO<sub>2</sub> surface at the grounded electrode at  $p = 1$  Pa and  $V_{\text{hf}} = 2000$  V.  $L = 5$  cm,  $f_{\text{lf}} = 400$  kHz,  $f_{\text{hf}} = 40$  MHz and  $V_{\text{lf}} = 10$  kV.

asymmetry is induced due to the presence of two different electrode materials.

Figure 12 shows the space and time averaged electron density as a function of  $p$  and  $V_{\text{hf}}$  for the scenario, where a Si surface at the powered electrode and a SiO<sub>2</sub> surface at the grounded electrode are used. The discharges are operated at  $f_{\text{lf}} = 400$  kHz,  $f_{\text{hf}} = 40$  MHz, and  $V_{\text{lf}} = 10$  kV. The results show a trend similar to that shown in figure 3, but a much lower plasma density is obtained at the same pressures and high-frequency voltages. This is caused by the lower SEECs at the powered electrode. A minimum neutral gas pressure of 0.6 Pa can be reached at a hf voltage of 2400 V.

In order to get a better insight into the effects of using different electrode surface materials on the charged particle dynamics and the formation of distribution functions, we pick one exemplary case and analyse the ionization dynamics and charged particle energy distribution functions at the electrodes in detail. This case is marked by a red circle in figure 12 and corresponds to a pressure of  $p = 1$  Pa and a high-frequency voltage of  $V_{\text{hf}} = 2000$  V. Figure 13 shows the axial profile of the time averaged electron and ion density for this case. Due to the higher emission coefficient for both  $\gamma$ -electrons and  $\delta$ -electrons at the grounded electrode, the maximum of the plasma density is shifted to this electrode. Consequently, a large sheath is generated at the powered electrode and a much smaller sheath is found adjacent to the grounded electrode.

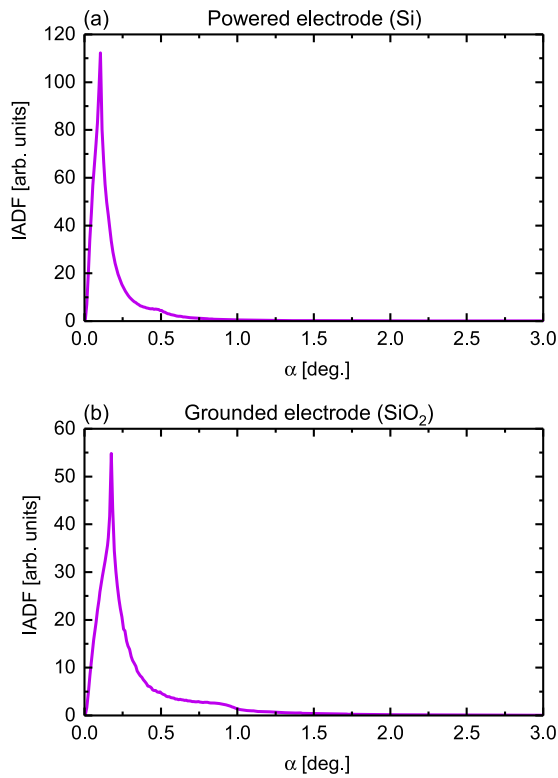


**Figure 17.** Ion angular distribution at the powered electrode (a) and at the grounded electrode (b) in a dual-frequency CCP with a Si surface at the powered electrode and a SiO<sub>2</sub> surface at the grounded electrode at  $p = 1$  Pa and  $V_{\text{hf}} = 2000$  V.  $L = 5$  cm,  $f_{\text{lf}} = 400$  kHz,  $f_{\text{hf}} = 40$  MHz and  $V_{\text{lf}} = 10$  kV.

Figure 14 shows the time averaged electron energy probability function (EPPF) collected within a 1 mm wide region centered at the density peak position in the plasma bulk for three selected pressures. Compared to the discharge configured with identical electrode materials, as shown in figure 4, the transition between the low and the high energy electron populations is at somewhat lower electron energies.

The discharge asymmetry induced by the presence of different electrode materials also leads to the generation of a DC self-bias voltage,  $\eta$ , of  $-5637$  V for this case despite the geometric reactor symmetry in the simulation. The formation of the DC self-bias can be understood based on a model introduced by Czarnetzki *et al* [95], which yields the following expression for the DC self-bias voltage:

$$\eta = -\frac{\tilde{\phi}_{\text{max}} + \varepsilon \tilde{\phi}_{\text{min}}}{1 + \varepsilon}. \quad (6)$$

Here,  $\tilde{\phi}_{\text{max}}$  and  $\tilde{\phi}_{\text{min}}$  is the global maximum and minimum of the driving voltage waveform, respectively, and  $\varepsilon$  is the symmetry parameter, which for a geometrically symmetric CCP is given by:

$$\varepsilon = \left| \frac{\hat{\phi}_{\text{sg}}}{\hat{\phi}_{\text{sp}}} \right| \approx \frac{\bar{n}_{\text{sp}}}{\bar{n}_{\text{sg}}}, \quad (7)$$

where  $\hat{\phi}_{\text{sg}}$ ,  $\hat{\phi}_{\text{sp}}$  are the maximum voltage drops across the sheath at the grounded and powered electrode, respectively,

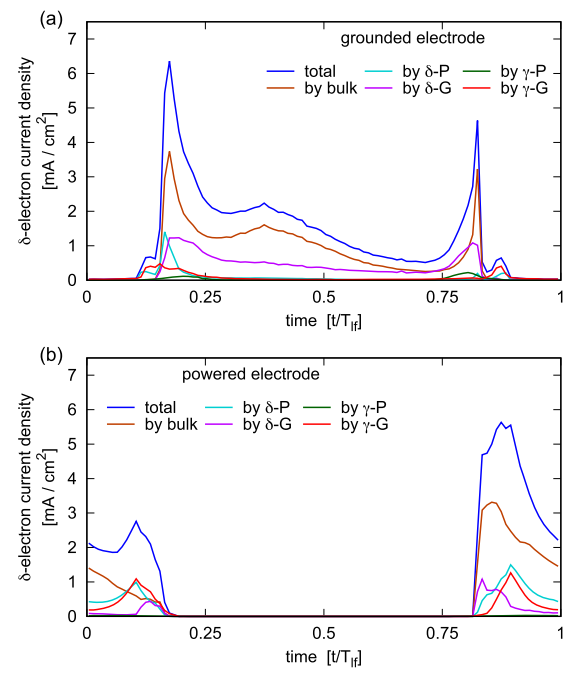


**Figure 18.** Current density of emitted  $\delta$ -electrons at the grounded (a) and powered electrode (b) as a function of time within the lf period without temporal resolution within the hf period. Different lines indicate the contribution of distinct groups of electrons to the generation of  $\delta$ -electrons at this electrode, i.e. the contributions of bulk,  $\delta$ -, and  $\gamma$ -electrons emitted from the powered (P) and grounded (G) electrodes are shown.  $p = 1$  Pa,  $L = 5$  cm,  $f_{\text{lf}} = 400$  kHz and  $f_{\text{hf}} = 40$  MHz,  $V_{\text{lf}} = 10$  kV and  $V_{\text{hf}} = 2000$  V, Si at the powered and SiO<sub>2</sub> at the grounded electrode.

and  $\bar{n}_{\text{sg}}$ ,  $\bar{n}_{\text{sp}}$  are the mean ion densities in the respective sheath.

For the dual-frequency driving voltage waveform used here,  $\tilde{\phi}_{\text{max}} \approx -\tilde{\phi}_{\text{min}} = \phi_0$ . Therefore:

$$\eta = -\phi_0 \frac{1 - \varepsilon}{1 + \varepsilon}. \quad (8)$$

In the presence of different electrode surface materials, the maximum of the plasma density profile is shifted towards the electrode, where the SEECs are higher (see figure 13). Thus, for the case, where these surface coefficients are larger at the SiO<sub>2</sub> grounded electrode,  $\bar{n}_{\text{sg}} > \bar{n}_{\text{sp}}$  and, therefore,  $\varepsilon < 1$  and  $\eta < 0$ , i.e. a negative self bias is generated. This explains the DC self-bias value of  $\eta = -5637$  V observed for the chosen discharge conditions. As  $\eta$  corresponds to the difference of the absolute values of the time averaged sheath voltages at the grounded and powered electrode, this means that the mean sheath voltage is much higher at the powered electrode. As  $\varepsilon < 1$ , the maximum sheath voltage is also higher at the powered compared to the grounded electrode. In combination with the lower plasma density adjacent to the powered electrode this results in a larger maximum sheath width and a longer duration of the sheath expansion at the powered compared to the grounded electrode. This is clearly observed in figure 15, which shows the spatio-temporal distribution of the electric field for these discharge conditions.

Consequently, positive ions bombard the powered electrode at much higher energies compared to the grounded electrode.

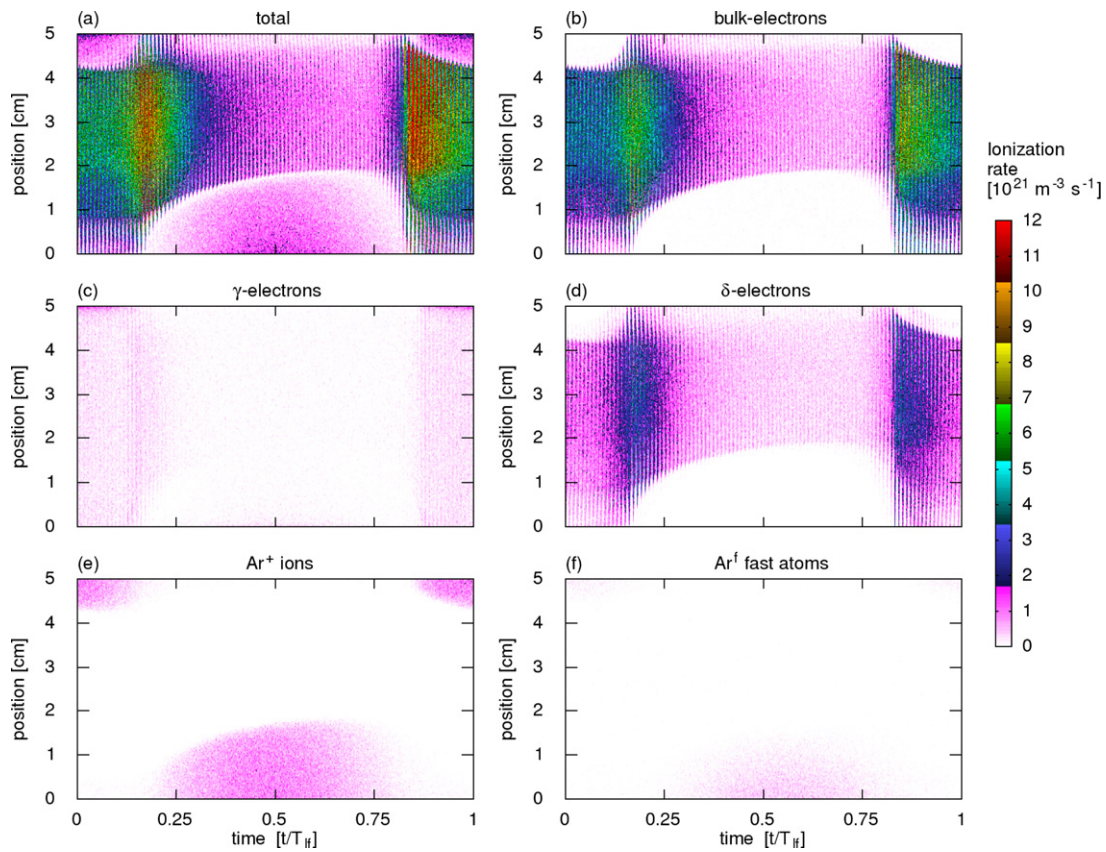


**Figure 19.** Spatio-temporal plots of the ionization rate generated by all particles (electrons, ions, fast neutrals) (a), bulk electrons (b),  $\gamma$ -electrons (c)  $\delta$ -electrons (d), ions (e), and fast atoms (f) in a dual-frequency CCP with a Si surface at the powered electrode and a  $\text{SiO}_2$  surface at the grounded electrode at  $p = 1$  Pa and  $V_{\text{hf}} = 2000$  V.  $L = 5$  cm,  $f_{\text{hf}} = 400$  kHz,  $f_{\text{lf}} = 40$  MHz and  $V_{\text{lf}} = 10$  kV.

This is illustrated in figure 16, which shows the ion energy distribution functions at both electrodes in the presence of different electrode surface materials. At the powered electrode maximum ion energies of about 16 keV are found, whereas the maximum ion energy at the grounded electrode is only about 4.5 keV. At both electrodes the ions bombard the surfaces essentially vertically as confirmed by the angular distribution functions displayed in figure 17. These results show that the electrode/wall materials have a significant influence on the ion distribution functions.

The presence of different ion bombardment energies, surface materials, and sheath voltages at both electrodes has significant consequences on the generation and acceleration of secondary electrons in the sheaths at both boundary surfaces. Despite the higher heavy particle energy at the powered compared to the grounded electrode, the effective heavy particle induced SEEC is lower at the powered electrode ( $\gamma_{\text{eff,P}} \approx 0.45$ ,  $\gamma_{\text{eff,G}} \approx 1.1$ ) due to the different surface material, which is characterized by a lower heavy particle induced SEEC at high incident particle energies. The lower ion flux at the powered electrode due to the shifted plasma density profile is another reason why fewer  $\gamma$ -electrons are generated at the powered electrode. The emitted SEs are accelerated towards the plasma bulk to much higher energies at the powered electrode due to the higher local sheath voltage. Due to the lower sheath potential at the grounded electrode, these  $\gamma$ -electrons generated at the powered electrode can overcome the sheath

potential at the grounded electrode and bombard this electrode during most of the low-frequency period.

Figure 18 shows the current density of  $\delta$ -electrons emitted at the grounded electrode (a) and at the powered electrode (b), as well as the contributions of each different electron group to the electron induced SEE as a function of time within the lf period without temporal resolution within the hf period. In principle, the mechanisms of  $\delta$ -electron generation at both electrodes are the same as discussed previously for the scenario, where two identical electrode materials are used (see figure 8 and the related discussion). Therefore, here only the differences compared to this reference case as a consequence of the presence of different electrode materials are discussed.

As a consequence of the asymmetry induced by the presence of different electrode surface materials the lf sheath is collapsed for a longer fraction of one lf period at the grounded compared to the powered electrode. Thus, electrons can reach the grounded electrode surface within a longer fraction of the lf period compared to the situation at the powered electrode and, thus,  $\delta$ -electrons are emitted within a longer time interval at the grounded electrode. At the powered electrode  $\gamma$ -electrons generated at the grounded electrode have a higher contribution to the generation of electron induced secondary electrons compared to the situation at the grounded electrode, because they arrive at lower energies, since the sheath voltage at the grounded electrode is lower. Although the  $\delta$ -coefficient

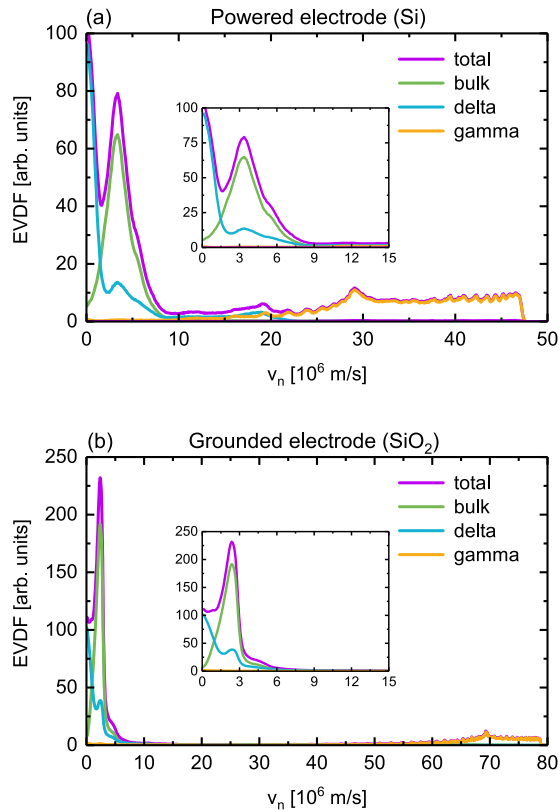


**Figure 20.** Electron velocity distribution (as a function of the velocity component normal to the surface) at the powered electrode (a) and at the grounded electrode (b) for all electrons (total), bulk electrons,  $\delta$ -electrons, and  $\gamma$ -electrons in a dual-frequency CCP with a Si surface at the powered electrode and a SiO<sub>2</sub> surface at the grounded electrode at  $p = 1$  Pa and  $V_{\text{hf}} = 2000$  V.  $L = 5$  cm,  $f_{\text{lf}} = 400$  kHz,  $f_{\text{hf}} = 40$  MHz and  $V_{\text{lf}} = 10$  kV.

of Si is lower compared to that of SiO<sub>2</sub>, more  $\delta$ -electrons are emitted from the powered electrode compared to the grounded electrode at the time of  $t/T_{\text{lf}} \approx 0.82$ . This is mainly caused by two reasons: (i) the smaller  $\delta$ -electron emission threshold for Si (5 eV vs 15 eV for SiO<sub>2</sub>) and (ii) the larger sheath at the powered electrode, which leads to a faster sheath collapse and, thus, a stronger reversed electric field, which accelerates bulk electrons to higher energies upon impact at the electrode surface. This finally leads to more  $\delta$ -electron emission, since the electron induced SEEC increases as a function of the electron energy below 300 eV.

Figure 19 shows the spatio-temporal distribution of the total ionization rate generated by all particles (electrons, ions, fast neutrals) as well as the ionization rate caused by different particle species. Due to the presence of different surface materials, a strong asymmetry is generated in the ionization profiles. Most of the ionization occurs during the first and the last quarter of each lf period, which correspond to the times of most efficient sheath expansion heating at the powered and grounded electrode, respectively. As the plasma density is higher near the grounded electrode, more ionization is observed during sheath expansion at the grounded electrode. In addition to this, a weak ionization maximum is observed at the powered electrode at about  $t/T_{\text{lf}} \approx 0.82$ , when the sheath starts to collapse. This is caused by the strong local electric field reversal caused

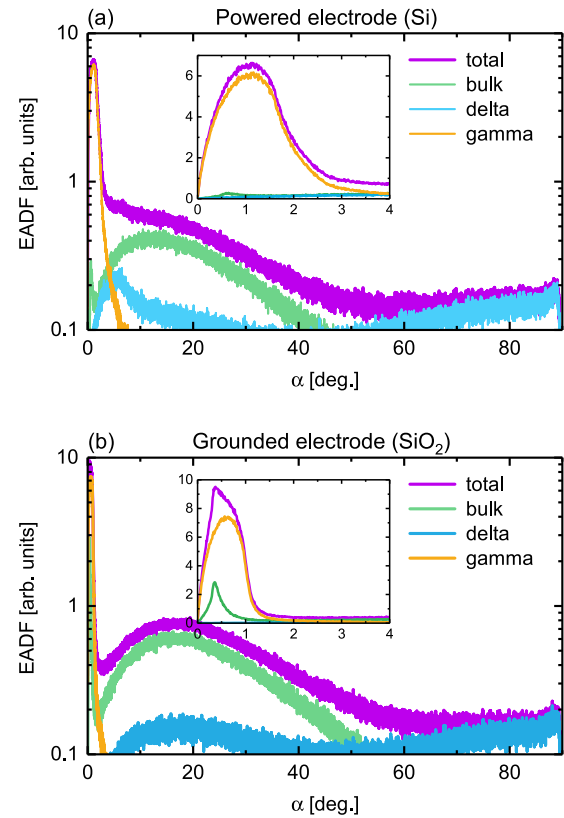


**Figure 21.** Electron angular distribution at the powered electrode (a) and at the grounded electrode (b) in a dual-frequency CCP with a Si surface at the powered electrode and a SiO<sub>2</sub> surface at the grounded electrode at 1 Pa and  $V_{\text{hf}} = 2000$  V.  $L = 5$  cm,  $f_{\text{lf}} = 400$  kHz,  $f_{\text{hf}} = 40$  MHz and  $V_{\text{lf}} = 10$  kV.

by the fast local sheath collapse. Compared to the case discussed in section 3.1, the contribution of secondary electrons to the total ionization is decreased due to the smaller SEECs at the powered Si electrode. The contribution of bulk electrons is increased to 67%, while the contribution of  $\delta$ -electrons is still important at 23%. The contribution of  $\gamma$ -electrons, ions, and fast neutrals to the total ionization is 5%, 4%, and 1%, respectively. Due to the generation of the large DC self-bias as a consequence of the surface material asymmetry, the sheath voltage at the powered electrode is extremely high. Thus,  $\gamma$ -electrons are accelerated to extremely high energies immediately after they are emitted from the surface. Therefore, the ionization caused by  $\gamma$ -electrons near the powered electrode is very weak during the phase of the local sheath expansion. At the grounded electrode more ionization caused by  $\gamma$ -electrons is observed during the phase of the local sheath expansion, since the local sheath voltage is lower.

Figure 20 shows the time averaged electron velocity distribution function at the powered electrode (a) and at the grounded electrode (b) in the presence of different electrode surface materials as a function of the velocity component normal to the surface,  $v_n$ . It is split into different groups of electrons, i.e. bulk-,  $\delta$ -, and  $\gamma$ -electrons. Similar to the results in figure 9(a), most of the  $\delta$ -electrons and bulk electrons reach the electrodes at low velocities. Different distribution functions are found at both electrodes due to the presence of

different surface materials. Due to the strong reversed electric field at the powered electrode, the bulk electrons arrive at this electrode with a higher energy compared to the grounded electrode, i.e. the corresponding peak of the bulk electron EVDF appears at about  $3.5 \times 10^6 \text{ ms}^{-1}$  at the powered electrode and at about  $2.5 \times 10^6 \text{ ms}^{-1}$  at the grounded electrode. The corresponding energies of bulk electrons at both the powered and the grounded electrode are high enough to generate a high number of  $\delta$ -electrons. This keeps the effect of  $\delta$ -electrons important in the discharge. The velocity distributions of  $\gamma$ -electrons at the electrodes are broad at high velocities. Due to the large sheath voltage at the powered electrode,  $\gamma$ -electrons can arrive at the grounded electrode at extremely high velocities of up to about  $8 \times 10^7 \text{ ms}^{-1}$ , while their maximum velocity at the powered electrode is only up to about  $4.8 \times 10^7 \text{ ms}^{-1}$  due to the lower sheath voltage at the grounded electrode.

The electron angular distribution functions at both electrodes are shown in figure 21. After being accelerated by the electric field inside the sheath at the opposing electrode, most  $\gamma$ -electrons bombard the respective electrode vertically. As a result of the larger sheath voltage at the powered electrode, the angle of incidence of  $\gamma$ -electrons at the grounded electrode is smaller.

We note that the self-consistent computation of the gas heating power and the gas temperature distribution show no significant rise of the gas temperature with respect to the constant electrode surface temperature ( $T_{\text{max}} < 1.1T_w$ ), for all cases studied.

Although the electron emission induced by metastable atoms and VUV photons are not part of the present model, it is possible to roughly estimate their contribution to electron emission based on event statistics of the corresponding excitation processes. We do this by taking into account the excitation events directly populating Ar metastable levels and the upper levels of the resonant VUV transitions. We find that in addition to electron induced processes,  $\text{Ar}^+$  ions and  $\text{Ar}^f$  fast atoms contribute with approx. 25% in total to the VUV excitation, which is a fairly high ratio compared to lower voltage conditions. Based on time-averaged event counts we can estimate the number of metastable atoms and photons reaching a surface. Assuming electron emission yields of 0.1 for both species the contribution to the total electron emission from all surfaces is found to be in the range of a few percent, which is not taken into account in our model. This low relative contribution is a consequence of the high voltage, low pressure conditions, where charged particles impact at the surfaces with significant energies resulting in very high effective electron emission yields. A detailed discussion of CCPs where electron emission induced by metastables and VUV photons have significant contributions is provided in [18].

#### 4. Conclusions

The spatio-temporally resolved charged particle dynamics and the formation of charged particle distribution functions at boundary surfaces were investigated by PIC/MCC simulations in a geometrically symmetric low pressure (0.5–1.5 Pa)

dual-frequency CCP operated at a low driving frequency of 400 kHz and a very high low-frequency driving voltage amplitude of 10 kV in combination with a second, much higher frequency of 40 MHz in argon gas. The choice of discharge conditions is motivated by HAR plasma etching, where extremely high ion bombardment energies are required at the wafer surface. The effects of secondary electron emission from the electrodes on the ionization dynamics and the formation of distribution functions were investigated in discharges, where (i) identical surface materials for both electrodes ( $\text{SiO}_2$ ) and (ii) different surface materials for both electrodes (powered: Si, grounded:  $\text{SiO}_2$ ) were used. These studies have been based on the implementation of realistic surface coefficients for ion, atom, and electron induced secondary electron emission in the simulations, which depend on the incident particle energy and the surface material.

Increasing the neutral gas pressure and the high-frequency driving voltage amplitude was found to enhance the plasma density. As a consequence of the high driving voltage amplitude and the low gas pressure the heavy particle energies at the electrodes can reach several keV. Thus, the effective heavy particle induced secondary electron emission coefficients can reach very high values of more than 2. The large number of  $\gamma$ -electrons is accelerated to high energies of several keV in the sheaths. Most of them are found to be too energetic to either cause ionization in the volume or to induce the emission of electron induced secondary electrons ( $\delta$ -electrons) at the opposite electrode. Ionization by  $\gamma$ -electrons is only observed in direct vicinity of the electrodes, where their energy is low enough to cause ionization. The strong electron emission at the electrodes was found to cause the generation of electric field reversals during the sheath collapse at the electrodes. As the positive ion flux to each electrode must be compensated on time average, these field reversals are required to pull electrons towards the surface and to ensure the flux balance to the electrodes in the presence of strong electron emission. As a consequence of the effective sheath expansion the electrode during sheath collapse by the reversed electric field, a high number of bulk electrons was found to bombard the electrodes at high energies during the local sheath collapse. These bombardment energies are high enough to cause strong emission of  $\delta$ -electrons due to bombardment of the electrodes by bulk electrons. In fact, most of the  $\delta$ -electrons were found to be induced by bulk electrons. These  $\delta$ -electrons contribute strongly to the ionization, i.e. up to 41% of the total ionization is directly caused by  $\delta$ -electrons. Neglecting such electron induced secondary electrons (such as done in most PIC/MCC simulations of CCPs), therefore, is highly problematic.

Changing one of the electrode surface materials from  $\text{SiO}_2$  to Si, while keeping  $\text{SiO}_2$  as surface material at the other electrode, was found to induce a strong discharge asymmetry. Due to the lower secondary electron emission coefficients of Si compared to  $\text{SiO}_2$  the maximum of the time averaged plasma density profile decreases significantly and shifts towards the electrode, where these surface coefficients are higher. Thus, the plasma density is higher at this electrode compared to the

other. This leads to the generation of a strong DC self-bias voltage of several kV, which, in turn, affects the sheath voltages at both electrodes. Adjacent to the electrode made of the material with lower secondary electron emission coefficients the mean and maximum sheath voltages are higher and the sheath is expanded for a longer fraction of the low-frequency period compared to the other electrode. Consequently, the ion energy distribution functions are very different at both electrodes, i.e. much higher ion bombardment energies are found at the electrode, where the emission coefficients are lower. At both electrodes vertical ion bombardment is observed. The different heavy particle bombardment energies at both electrodes as a consequence of this electrode material asymmetry also lead to different dynamics of the secondary electron emission at both electrodes. All these phenomena affect the spatio-temporal ionization dynamics, which turns out to be asymmetric both in space and time under such discharge conditions. Finally, the formation of electron velocity and angular distribution functions at the electrodes was also studied.  $\delta$ - and bulk electrons were found to bombard the electrodes mostly at low energies with a broad distribution of the angle of incidence. In contrast to these groups of electrons and due to the large sheath voltages,  $\gamma$ -electrons reach the electrodes at very high energies and at small angles relative to the surface normal. Generally, the charged particle distribution functions will be different at both electrodes, if different surface materials are used. Consequently, our simulations predict that these distribution functions can be tuned by carefully choosing these surface materials.

Our results show that the ionization dynamics in CCPs operated at very high voltage, at low-frequency and at low gas pressure are different from classical CCPs operated at lower voltages and higher frequencies. The emission of secondary electrons, including electron induced secondary electrons, is of key importance and, therefore, must be implemented realistically in simulations of such discharges. Moreover, kinetic simulations should be performed, since non-local effects play an important role. We expect our results to be relevant for HAR plasma etching, since they provide a fundamental basis for knowledge based process optimization. Clearly, additional investigations of more complex gas mixtures and reactor geometries are required in the future.

## Acknowledgments

This work is supported by the Samsung Electronics University R & D program [Control of electron distribution functions in dielectric plasma etching by voltage waveform tailoring to prevent surface charging inside etch features] and the China Scholarship Council (No. 201906060024). Zoltán Donkó, Aranka Derzsi, and Peter Hartmann gratefully acknowledge financial support from the Hungarian Office for Research, Development and Innovation under NKFIH grants K-119357, K-134462, FK-128924 and K-132158. Support by the János Bolyai Research Fellowship of the Hungarian Academy of Sciences (A Derzsi) is acknowledged. Thomas Mussenbrock

gratefully acknowledges financial support from the German Research Foundation via MU 2332/6-1.

## ORCID iDs

P Hartmann  <https://orcid.org/0000-0003-3572-1310>  
 L Wang  <https://orcid.org/0000-0002-3106-2779>  
 B Berger  <https://orcid.org/0000-0001-7053-2545>  
 S Wilczek  <https://orcid.org/0000-0003-0583-4613>  
 T Mussenbrock  <https://orcid.org/0000-0001-6445-4990>  
 Z Donkó  <https://orcid.org/0000-0003-1369-6150>  
 A Derzsi  <https://orcid.org/0000-0002-8005-5348>  
 J Schulze  <https://orcid.org/0000-0001-7929-5734>

## References

- [1] Lieberman M A and Lichtenberg A J 2005 *Principles of Plasma Discharges and Materials Processing* 2nd edn (New York: Wiley)
- [2] Chabert P and Braithwaite N 2011 *Physics of Radio-Frequency Plasmas* (Cambridge: Cambridge University Press)
- [3] Makabe T and Petrovic Z L 2014 *Plasma Electronics: Applications in Microelectronic Device Fabrication* 2nd edn (Boca Raton: CRC Press)
- [4] Huang S, Shim S, Nam S K and Kushner M J 2020 *J. Vac. Sci. Technol. A* **38** 023001
- [5] Huang S, Huard C, Shim S, Nam S K, Song I C, Lu S and Kushner M J 2019 *J. Vac. Sci. Technol. A* **37** 031304
- [6] Zhang Y, Kushner M J, Moore N, Pribyl P and Gekelman W 2013 *J. Vac. Sci. Technol. A* **31** 061311
- [7] Zhang Y, Kushner M J, Sriraman S, Marakhtanov A, Holland J and Paterson A 2015 *J. Vac. Sci. Technol. A* **33** 031302
- [8] Kitajima T, Takeo Y and Makabe T 1999 *J. Vac. Sci. Technol. A* **17** 2510
- [9] Tatsumi T, Matsui M, Okigawa M and Sekine M 2000 *J. Vac. Sci. Technol. B* **18** 1897
- [10] Tsai W, Mueller G, Lindquist R, Frazier B and Vahedi V 1996 *J. Vac. Sci. Technol. B* **14** 3276
- [11] Oh S G, Park K S, Lee Y J, Jeon J H, Choe H H and Seo J H 2014 *Adv. Mater. Sci. Eng.* **2014** 608608
- [12] Jeon M H, Yang K C, Kim K N and Yeom G Y 2015 *Vacuum* **121** 294–9
- [13] Ishikawa K et al 2017 *Japan. J. Appl. Phys.* **56** 06HA02
- [14] Pedersen M and Huff M 2017 *J. Microelectromech. Syst.* **26** 448–55
- [15] He T, Wang Z, Zhong F, Fang H, Wang P and Hu W 2019 *Adv. Mater. Technol.* **4** 1900064
- [16] Daksha M, Derzsi A, Wilczek S, Trieschmann J, Mussenbrock T, Awakowicz P, Donkó Z and Schulze J 2017 *Plasma Sources Sci. Technol.* **26** 085006
- [17] Derzsi A, Korolov I, Schüngel E, Donkó Z and Schulze J 2015 *Plasma Sources Sci. Technol.* **24** 034002
- [18] Braginsky O, Kovalev A, Lopaev D, Proshina O, Rakhimova T, Vasilieva A, Voloshin D and Zyryanov S 2011 *J. Phys. D: Appl. Phys.* **45** 015201
- [19] Lafleur T, Schulze J and Donkó Z 2019 *Plasma Sources Sci. Technol.* **28** 040201
- [20] Sun J Y, Wen D Q, Zhang Q Z, Liu Y X and Wang Y N 2019 *Phys. Plasmas* **26** 063505
- [21] Proto A and Gudmundsson J T 2018 *Atoms* **6** 65
- [22] Liu G H, Wang X Y, Liu Y X, Sun J Y and Wang Y N 2018 *Plasma Sources Sci. Technol.* **27** 064004
- [23] Wang L, Wen D Q, Zhang Q Z, Song Y H, Zhang Y R and Wang Y N 2019 *Plasma Sources Sci. Technol.* **28** 055007

- [24] Belenguer P and Boeuf J P 1990 *Phys. Rev. A* **41** 4447–59
- [25] Schulze J, Heil B G, Luggenhölscher D and Czarnetzki U 2008 *IEEE Trans. Plasma Sci.* **36** 1400–1
- [26] Schulze J, Heil B G, Luggenhölscher D, Brinkmann R P and Czarnetzki U 2008 *J. Phys. D: Appl. Phys.* **41** 195212
- [27] Schulze J, Kampschulte T, Luggenhölscher D and Czarnetzki U 2007 *J. Phys.: Conf. Series* **86** 012010
- [28] Booth J P, Curley G, Marić D and Chabert P 2009 *Plasma Sources Sci. Technol.* **19** 015005
- [29] Schulze J, Donkó Z, Schüngel E and Czarnetzki U 2011 *Plasma Sources Sci. Technol.* **20** 045007
- [30] Donkó Z, Schulze J, Hartmann P, Korolov I, Czarnetzki U and Schüngel E 2010 *Appl. Phys. Lett.* **97** 081501
- [31] Derzsi A, Horváth B, Korolov I, Donkó Z and Schulze J 2019 *J. Appl. Phys.* **126** 043303
- [32] Phelps A V, Pitchford L C, Pédoussat C and Donkó Z 1999 *Plasma Sources Sci. Technol.* **8** B1–2
- [33] Horváth B, Daksha M, Korolov I, Derzsi A and Schulze J 2017 *Plasma Sources Sci. Technol.* **26** 124001
- [34] Horváth B, Schulze J, Donkó Z and Derzsi A 2018 *J. Phys. D: Appl. Phys.* **51** 355204
- [35] Campanell M D, Khrabov A V and Kaganovich I D 2012 *Phys. Rev. Lett.* **108** 255001
- [36] Campanell M D 2013 *Phys. Rev. E* **88** 033103
- [37] Proto A and Gudmundsson J T 2018 *Plasma Sources Sci. Technol.* **27** 074002
- [38] Greb A, Niemi K, O’Connell D and Gans T 2013 *Appl. Phys. Lett.* **103** 244101
- [39] Gudmundsson J T, Kawamura E and Lieberman M A 2013 *Plasma Sources Sci. Technol.* **22** 035011
- [40] Daksha M, Derzsi A, Mujahid Z, Schulenberg D, Berger B, Donkó Z and Schulze J 2019 *Plasma Sources Sci. Technol.* **28** 034002
- [41] Korolov I, Derzsi A, Donkó Z and Schulze J 2013 *Appl. Phys. Lett.* **103** 064102
- [42] Lafleur T, Chabert P and Booth J P 2013 *J. Phys. D: Appl. Phys.* **46** 135201
- [43] Evans M W and Harlow F H 1957 The particle-in-cell method for hydrodynamic calculations *Technical Report LA-2139* Los Alamos Scientific Laboratory Los Alamos New Mexico URL <https://apps.dtic.mil/dtic/tr/fulltext/u2/a384618.pdf>
- [44] Birdsall C and Langdon A 1991 *Plasma Physics via Computer Simulation* (Boca Raton: CRC Press)
- [45] Birdsall C K 1991 *IEEE Trans. Plasma Sci.* **19** 65–85
- [46] Hockney R and Eastwood J 1988 *Computer Simulation Using Particles* (New York: Taylor and Francis)
- [47] Diomede P, Capitelli M and Longo S 2005 *Plasma Sources Sci. Technol.* **14** 459–66
- [48] Matyash K, Schneider R, Taccogna F, Hatayama A, Longo S, Capitelli M, Tskhakaya D and Bronold F X 2007 *Contrib. Plasma Phys.* **47** 595–634
- [49] Donkó Z 2011 *Plasma Sources Sci. Technol.* **20** 024001
- [50] Donkó Z, Schulze J, Czarnetzki U, Derzsi A, Hartmann P, Korolov I and Schüngel E 2012 *Plasma Phys. Control. Fusion* **54** 124003
- [51] Sun A, Becker M M and Loffhagen D 2016 *Comput. Phys. Commun.* **206** 35–44
- [52] Surendra M and Graves D B 1991 *IEEE Trans. Plasma Sci.* **19** 144–57
- [53] Verboncoeur J P 2005 *Plasma Phys. Control. Fusion* **47** A231–60
- [54] Mertmann P, Eremin D, Mussenbrock T, Brinkmann R P and Awakowicz P 2011 *Comput. Phys. Commun.* **182** 2161–7
- [55] Claustre J, Chaudhury B, Fubiani G, Paulin M and Boeuf J P 2013 *IEEE Trans. Plasma Sci.* **41** 391–9
- [56] Hur M Y, Kim J S, Song I C, Verboncoeur J P and Lee H J 2019 *Plasma Res. Express* **1** 015016
- [57] Serikov V V and Nanbu K 1997 *J. Appl. Phys.* **82** 5948–57
- [58] COP database [www.lxcat.net](http://www.lxcat.net), retrieved on January 10, 2020
- [59] McEachran R and Stauffer A 2014 *Eur. Phys. J. D* **68** 153
- [60] Hayashi database [www.lxcat.net](http://www.lxcat.net), retrieved on January 10, 2020
- [61] Hayashi M 2003 Bibliography of electron and photon cross sections with atoms and molecules published in the 20th century—argon *Technical Report NIFS-DATA-072* National Institute for Fusion Science Toki Gifu p509 Japan URL <http://nifs.ac.jp/report/NIFS-DATA-072.pdf-5292>
- [62] Phelps A V 1991 *J. Phys. Chem. Ref. Data* **20** 557–73
- [63] de Heer F J, Jansen R H J and van der Kaay W 1979 *J. Phys. B: At. Mol. Phys.* **12** 979–1002
- [64] Karim K R and Jain A 1989 *Phys. Scr.* **39** 238–42
- [65] Phelps A V 1994 *J. Appl. Phys.* **76** 747–53
- [66] Raju G G 2004 *IEEE Trans. Dielectr. Electr. Insul.* **11** 649–73
- [67] Pitchford L C et al 2013 *J. Phys. D: Appl. Phys.* **46** 334001
- [68] Okhrimovskyy A, Bogaerts A and Gijbels R 2002 *Phys. Rev. E* **65** 037402
- [69] Fiala A 1995 Modélisation numérique bidimensionnelle d’une décharge luminescente à basse pression *PhD Thesis* (Toulouse Cedex:L’Université Paul Sabatier de Toulouse C.P.A.T)
- [70] Opal C B, Peterson W K and Beaty E C 1971 *J. Chem. Phys.* **55** 4100–6
- [71] Yoshida S, Phelps A V and Pitchford L C 1983 *Phys. Rev. A* **27** 2858–67
- [72] Donkó Z 1998 *Phys. Rev. E* **57** 7126–37
- [73] Phelps A V and Petrovic Z L 1999 *Plasma Sources Sci. Technol.* **8** R21–44
- [74] Rösler M 1991 *Particle Induced Electron Emission I* (Springer Tracts in Modern Physics) (Berlin: Springer)
- [75] Sydorenko D 2006 Particle-in-cell simulations of electron dynamics in low pressure discharges with magnetic fields *PhD Thesis* University of Saskatchewan Saskatoon, Canada
- [76] Vaughan J R M 1989 *IEEE Trans. Electron Devices* **36** 1963–7
- [77] Vaughan J R M 1993 *IEEE Trans. Electron Devices* **40** 830
- [78] Seiler H 1983 *J. Appl. Phys.* **54** R1–18
- [79] Shatalov V, Panchenko O, Artamonov O, Vinogradov A and Terekhov A 1988 *Solid State Commun.* **68** 719–22
- [80] Walker C, El-Gomati M, Assa’d A and Zdražil M 2008 *Scanning* **30** 365–80
- [81] Lin Y and Joy D C 2005 *Surf. Interface Anal.* **37** 895–900
- [82] Turner M M 2006 *Phys. Plasmas* **13** 033506
- [83] Thomas L 1949 Elliptic problems in linear difference equations over a network *Technical Report Watson Sci. Comput. Lab.* Columbia University New York
- [84] Younglove B A and Hanley H J M 1986 *J. Phys. Chem. Ref. Data* **15** 1323–37
- [85] Bird G A 1994 *Molecular Gas Dynamics and the Direct Simulation of Gas Flows* (Oxford: Clarendon)
- [86] Sazhin S and Serikov V 1997 *Planet. Space Sci.* **45** 361–8
- [87] Gans T, Schulze J, O’Connell D, Czarnetzki U, Faulkner R, Ellingboe B and Turner M 2006 *Appl. Phys. Lett.* **89** 261502
- [88] Schulze J, Schüngel E, Donkó Z and Czarnetzki U 2010 *J. Phys. D* **43** 225201
- [89] Schulze J, Donkó Z, Derzsi A, Korolov I and Schüngel E 2015 *Plasma Sources Sci. Technol.* **24** 015019
- [90] Schulze J, Donkó Z, Lafleur T, Wilczek S and Brinkmann R P 2018 *Plasma Sources Sci. Technol.* **27** 055010
- [91] Zhang Q Z, Wang Y N and Bogaerts A 2014 *J. Appl. Phys.* **115** 223302
- [92] Wen D Q, Liu W, Gao F, Lieberman M A and Wang Y N 2016 *Plasma Sources Sci. Technol.* **25** 045009
- [93] Wen D Q, Zhang Y R, Lieberman M A and Wang Y N 2017 *Plasma Processes Polym.* **14** 1600100
- [94] Kushner M J 1985 *J. Appl. Phys.* **58** 4024–31
- [95] Czarnetzki U, Schulze J, Schüngel E and Donkó Z 2011 *Plasma Sources Sci. Technol.* **20** 024010